A climate model-informed nonstationary stochastic rainfall generator for design flood analyses in continental-scale river basins

Yuan Liu[1], Daniel B. Wright[1], and David J. Lorenz[2]

[1]Department of Civil and Environmental Engineering, University of Wisconsin-Madison, Madison, WI, USA.

[2]Center for Climatic Research, University of Wisconsin-Madison, Madison, WI, USA.

Corresponding author: Yuan Liu (yliu2232@wisc.edu)

Key Points:

- A nonstationary stochastic rainfall generator driven by water vapor transport is proposed to simulate storms in the Mississippi Basin
- 1,000 synthetic years of precipitation events were simulated based on large-scale atmospheric variables from a global climate model
- Good agreement was found between distributions of simulated and reference annual precipitation maxima

Abstract

Existing stochastic rainfall generators (SRGs) are typically limited to relatively small domains due to spatial stationarity assumptions, hindering their usefulness for flood studies in large basins. This study proposes StormLab, an SRG that simulates precipitation events at 6-hour and 0.03° resolution in the Mississippi River Basin (MRB). The model focuses on winter and spring storms caused by strong water vapor transport from the Gulf of Mexico—the key flood-generating storm type in the basin. The model generates anisotropic spatiotemporal noise fields that replicate local precipitation structures from observed data. The noise is transformed into precipitation through parametric distributions conditioned on large-scale atmospheric fields from a climate model, reflecting both spatial and temporal nonstationarity. StormLab can produce multiple realizations that reflect the uncertainty in fine-scale precipitation arising from a specific large-scale atmospheric environment. Model parameters were fitted for each month from December-May, based on storms identified from 1979-2021 ERA5 reanalysis data and AORC precipitation. Validation showed good consistency in key storm characteristics between StormLab simulations and AORC data. StormLab then generated 1,000 synthetic years of precipitation events based on 10 CESM2 ensemble simulations. Empirical return levels of simulated annual maxima agreed well with AORC data and displayed bounded tail behavior. To our knowledge, this is the first SRG simulating nonstationary, anisotropic high-resolution precipitation over continental-scale river basins, demonstrating the value of conditioning such stochastic models on large-scale atmospheric variables. The simulated events provide a wide range of extreme precipitation scenarios that can be further used for design floods in the MRB.

1 Introduction

The Mississippi River Basin (MRB) has experienced multiple extreme floods throughout history, including the Spring 1927 Flood (J. A. Smith & Baeck, 2015), the Great Flood of 1993 (Dirmeyer & Brubaker, 1999; Dirmeyer & Kinter III, 2009), and the June 2008 Midwest Flood (Dirmeyer & Kinter III, 2009; Budikova et al., 2010). These floods were each caused by sequences of severe large-scale rainstorms, all associated with strong water vapor transport from the Gulf of Mexico (Moore et al., 2012; Lavers & Villarini, 2013; Su et al., 2023). The project design flood was developed to estimate the maximum possible peak discharge and water levels in the lower MRB, providing guidelines for flood protection infrastructure and management (Gaines et al., 2019). Historical records of extreme rainstorms were placed in sequences, with modest perturbations to their timing, location, and severity to create hypothetical worst-case rainstorm scenarios (V. A. Myers, 1959). Of these, Hypo-Flood 58A, consisting of the rainstorm in January 1937 followed shortly by rainstorms in January 1950 and then February 1938, produced the largest discharge on the lower Mississippi River and has been used as the design flood since 1955 (Lewis et al., 2019; McWilliams & Hayes, 2017). However, this approach is not without limitations, including using a limited rainstorm record (i.e., pre-1950s) and providing only one worst-case scenario, rather than a range of possible outcomes with occurrence probabilities. With growing evidence that rainstorms are intensifying under future climate change (e.g., Ban et al., 2015; Fischer & Knutti, 2016; Matte et al., 2021; Fowler et al., 2021), historical design floods may fail to reflect the range of possible scenarios and may underestimate future risks (Wright et al., 2014; Yu et al., 2020).

In principle, stochastic rainfall generators (SRGs) can generate synthetic precipitation data that extend short observation records and provide a wide range of extreme scenarios to support flood risk management (Wilks & Wilby, 1999; Ailliot et al., 2015; Benoit et al., 2018). SRGs be categorized into three main types based on their simulation dimensions: point or area-averaged models, multi-site models, and space-time models. We will focus on the last type, which generates spatiotemporal precipitation data over regular grids. Reviews of other model types can be found in, e.g., Waymire & Gupta (1981), Mehrotra et al. (2006), and Qin (2011).

Existing space-time SRGs can be further classified into three major categories: 1) cluster-based models, 2) multifractal models, and 3) meta-Gaussian models. These categories are briefly reviewed here. Cluster-based models conceptualize the precipitation system as a hierarchical organization in which groups of small rain "cells" (~10-50 km^2) are embedded within large rainband areas (~10^3-10^4 km^2, e.g., Waymire et al., 1984). These models simulate rainband centers using Poisson processes, with elliptical rain cells randomly generated around each rainband following a clustered point process (e.g., Chen et al., 2021). Properties of these rain cells, including intensity, lifetime, area, and orientation are modeled via distributions fitted to observed data (Northrop, 1998). Total precipitation intensity at any location is calculated by summing the contributions from all existing (and possibly overlapping) rain cells. Cluster-based models were originally developed to simulate precipitation time series at single points (i.e., Neyman-Scott and Bartlett-Lewis models, Rodriguez-Iturbe et al., 1997) and later expanded for space-time simulations through work by Le Cam (1961), Waymire et al. (1984), Cowpertwait (1995), Northrop (1998), and others. Recent improvements include randomizing model parameters (Kaczmarska et al., 2014; Onof & Wang, 2020) and applying non-homogenous Poisson processes for rain cell arrivals (Burton et al., 2010). This modeling approach attempts to mimic the physical organization of precipitation systems and enables analytical derivation for key precipitation properties like moments and spatial correlation (Cowpertwait, 1995; Leonard et al., 2008). However, cluster-based models struggle to fully describe the precipitation statistical structure across scales (Foufoula-Georgiou & Krajewski, 1995) and typically lack dependence modeling between precipitation properties, e.g., rain cell duration and intensity, with implications for simulating extremes (Paschalis et al., 2013; Chen et al., 2021). The multi-level model structure also introduces many parameters, increasing model calibration difficulty (Jothityangkoon et al., 2000).

Multifractal models were developed based on empirical evidence that precipitation systems exhibit similar statistical properties across different temporal and spatial scales (i.e., scale invariance, see Schertzer & Lovejoy, 1987; Gupta & Waymire, 1993; Menabde et al., 1997). A common modeling approach, known as the discrete multiplicative random cascade (MRC), involves recursively subdividing the simulation domain into small squares and multiplying the precipitation intensity in each square by a random weight drawn from a fitted distribution (Sharma et al., 2007; Serinaldi, 2010; Rupp et al., 2012). A similar process is applied along the time dimension using a different dividing factor to account for anisotropy between space and time(Marsan et al., 1996; Veneziano et al., 2006). Other model variations include continuous MRC (Marsan et al., 1996), temporal Markov chain coupled with spatial MRC (Over & Gupta, 1996; Jothityangkoon et al., 2000), and rainfall cascade decomposition (Seed et al., 2013; Raut et al., 2019). Multifractal models aim to reflect precipitation physical structures and require fewer parameters than cluster-based models (Raut et al., 2018). Nevertheless, these models assume that precipitation fields are spatially isotropic and only represent limited types of space-time scaling

properties. These assumptions can introduce bias when precipitation does not exhibit perfect invariance over different temporal and spatial scales (Serinaldi, 2010).

Meta-Gaussian models represent precipitation evolution by simulating an underlying 2D Gaussian noise field that attempts to mimic the spatiotemporal correlation structure of actual precipitation (Baxevani & Lennartsson, 2015). This noise field is then transformed into precipitation amounts using a non-linear function, often a parametric precipitation distribution, generating simulations that are statistically consistent with observed precipitation (Mascaro et al., 2023). Meta-Gaussian models have become increasingly popular in recent years (Vischel et al., 2011; Sigrist et al., 2012; Papalexiou et al., 2021), with major differences in how they represent precipitation spatial structures. Approaches include parametric covariance functions (Paschalis et al., 2013; Papalexiou, 2018), turning band methods (Leblois & Creutin, 2013), fast Fourier transforms (FFTs, Nerini et al., 2017), stochastic partial differential equations (Fuglstad et al., 2015), and kernel convolutions (Fouedjio et al., 2016). A key advantage of meta-Gaussian models is their flexibility in modeling precipitation distributions and spatiotemporal dependence structures, which can yield improved extreme value simulations compared to other SRGs. However, they often involve many parameters and high computational demand for large-scale simulations (Paschalis et al., 2013; Papalexiou & Serinaldi, 2020). Modeling temporal autocorrelation also remains challenging due to its dependence on storm movement and on spatial correlation (Storvik et al., 2002). Beyond the three major categories described, there also exist some other space-time rainfall generators such as variogram-based simulations (Schleiss et al., 2014) and deep learning models (e.g., Zhang et al., 2020; Leinonen et al., 2021; Rampal et al., 2022).

Most existing SRGs assume the precipitation field is second-order stationary, i.e., the mean of precipitation is constant across the region, with covariance between two grid cells depending only on their separation distance rather than their absolute locations (Fuglstad et al., 2015; Benoit et al., 2018; Hristopulos, 2020). This limits simulation domains to relatively small areas where precipitation can be considered homogeneous (Vischel et al., 2011; Schleiss et al., 2014; Papalexiou et al., 2021). Such an assumption precludes the usage of such SRGs for simulating extreme precipitation over continental-scale basins like the MRB. Extreme rainstorms in large basins are likely to arise from different types of weather systems (e.g., tropical cyclones, extratropical cyclones, mesoscale convective systems) exhibiting distinct precipitation distributions and correlation structures (Barlow et al., 2019; B. Liu et al., 2020; Schumacher & Rasmussen, 2020). Precipitation distributions also vary spatially, with regions near moisture sources or subject to orographic lifting showing higher means and variances (Hitchens et al., 2013; Marra et al., 2022). Nonstationarity in spatial correlation structures is clearly evident in high-resolution precipitation observations, with patterns varying significantly within different parts of large weather systems like extratropical cyclones (Niemi et al., 2014; Nerini et al., 2017). Moreover, observed increases in extreme precipitation due to anthropogenic climate change suggest temporal nonstationarity in precipitation properties, challenging the usage of temporally stationary distributions of precipitation amount (Pan et al., 2016; Gori et al., 2022). Consequently, stationary SRGs will struggle in several key respects to represent the strong spatiotemporal nonstationarity of extreme precipitation within a large basin. Several efforts have been made to model nonstationary precipitation fields (e.g., Fuglstad et al., 2015; Fouedjio et al., 2016; Nerini et al., 2017; Fouedjio, 2017), but to our knowledge, no SRG has been developed to simulate nonstationary precipitation fields for a basin as large as the MRB.

In this study, we propose the Space-Time nOnstationary Rainfall Model for Large Area Basins (StormLab), an SRG that generates 6-hour, 0.03° resolution rainstorms over the MRB. Following the meta-Gaussian framework, the model generates spatiotemporally correlated noise fields and converts them to actual precipitation patterns via precipitation distribution functions. Unlike some other SRGs that simulate precipitation without conditioning on additional atmospheric variables, StormLab performs conditional simulations where precipitation distributions vary across space and time, dependent on large-scale atmospheric variables from global climate models (GCMs). Such conditioning incorporates spatial and temporal nonstationarity of precipitation and realistically represents how local-scale precipitation is embedded within and driven by the larger-scale atmospheric environment. Nonstationarity in the spatial correlation of precipitation is further addressed by replicating local correlation structures from precipitation observations using a "local window" FFT approach. StormLab was used to generate 1,000 synthetic years of winter and spring rainstorms conditioned on GCM outputs. StormLab can alternatively be understood as a stochastic downscaling approach, i.e., establishing statistical relationships between coarse GCM data and local precipitation observations. In this study, "rainstorm" is used to denote a heavy precipitation event, though it may contain snow or mixed-phase precipitation. All input data and stochastic simulations consider liquid water equivalent, without distinction of precipitation phase. The remainder of the paper is organized as follows: Section 2 describes the study basin and datasets. Section 3 details the proposed methods. Results are shown in Section 4, followed by discussion in Section 5. A summary and conclusions are provided in Section 6.

2 Study Site and Data Processing

The Mississippi River Basin, the largest watershed in North America, has a drainage area of 3.2 million km^2 and consists of five major subbasins: the Arkansas-Red, Missouri, Upper Mississippi, Ohio-Tennessee, and Lower Mississippi (Figure 1a). Major flood events occur during winter and spring (December-May), resulting in significant socioeconomic impacts across the basin (Myers & White, 1993; Mutel, 2010; A. B. Smith & Katz, 2013). Due to the basin's large and complex drainage network, the locations and spatiotemporal patterns of heavy precipitation greatly influence flood responses and damages throughout the basin (Su et al., 2023).

The Analysis of Record for Calibration (AORC) dataset provides reference precipitation data at 6-hour, 0.03° resolution over the MRB from 1979-2021. The dataset was created by combining hourly NLDAS-2 and Stage IV precipitation data (Fall et al., 2023), which we resampled to 6-hour intervals in this study. ERA5 reanalysis, produced by the European Centre for Medium-Range Weather Forecast (ECMWF), provides hourly, 0.25° fields of large-scale atmospheric variable fields (Hersbach et al., 2018); we used precipitation, precipitable water, integrated water transport (IVT), and 850 hPa winds over the study region from 1979-2021. ERA5 fields were resampled to 6-hour intervals and spatially upscaled to match the resolution of the CESM2 dataset (described next), using the Python package "xESMF" (Zhuang et al., 2020). The CESM2 Large-Ensemble Project provides 100 ensemble members of historical (1850-2014) and future projection (2015-2100; SSP3-7.0 scenario) simulations using the CESM2 model (Danabasoglu et al., 2020; Rodgers et al., 2021). We used ten ensemble members from 1951-2050, equivalent to

1,000 years of atmospheric simulations, from which precipitation, precipitable water, IVT, and 850 hPa winds were retrieved at approximately 1-degree resolution and 6-hour intervals. The CESM2 large-scale atmospheric variables were bias-corrected against ERA5 data for each season using the CDF-t method (M. Vrac et al., 2012; see Supporting Information S1).

3 Methods

3.1 Rainstorm Identification

Rainstorms associated with strong water vapor transport were identified over the MRB in ERA5 and CESM2. First, we applied a storm tracking method STARCH (Y. Liu & Wright, 2022b) to identify periods of intense water vapor transport over the tracking domain (29-50° N, 79-113° W, Figure 1a). STARCH applies a high threshold (500 kg $m^{-1}s^{-1}$) to the IVT fields to identify regions of intense water vapor transport at each time step. These regions were then expanded to a lower threshold (250 kg $m^{-1}s^{-1}$) to capture more IVT areas. The identified IVT objects were tracked across time by computing the overlap ratio between objects at consecutive time steps. If the overlap ratio exceeds 0.2, the objects were considered the same IVT event and tracked through time (Figure 1a, see Supporting Information S2 for more details). These IVT events were considered as indicators for individual rainstorms and associated with concurrent precipitation, precipitable water, and wind speed fields from ERA5/CESM2 data (e.g., Figure 1b). To focus on extreme events that potentially lead to large-scale flooding, we only selected rainstorms with precipitation covering >10% of the basin for more than 24 hours. The starting and ending periods of a rainstorm were also cropped if the precipitation coverage was <10% of the basin. For ERA5 data, we identified 1,088 rainstorms from December-May during 1979-2021 and associated AORC precipitation (Figure 1c). For CESM2, we identified 26,166 rainstorms over the 1,000 years.

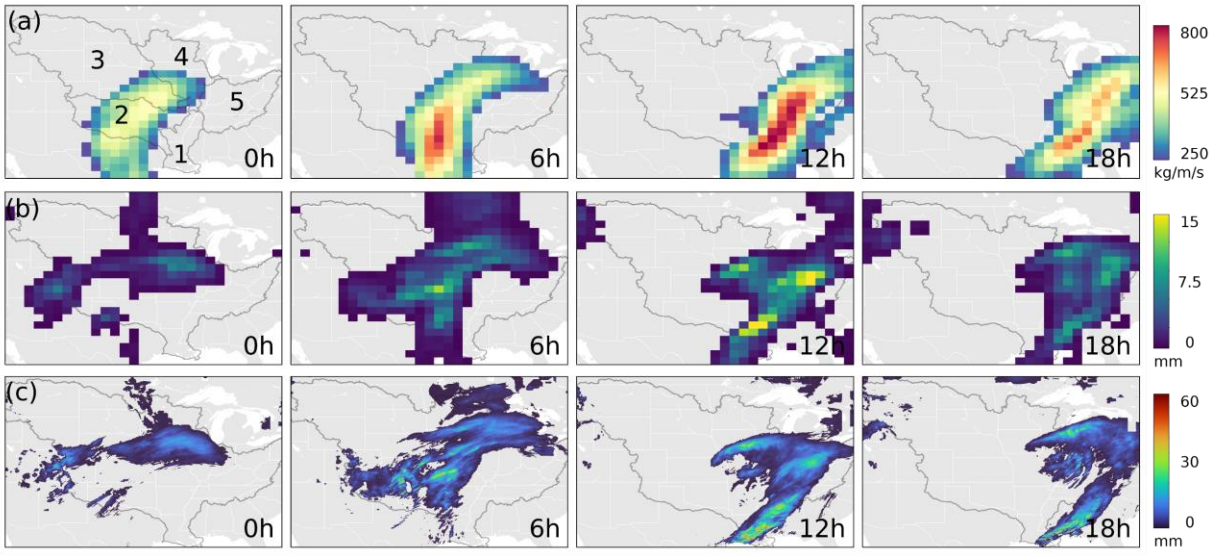

Figure 1. STARCH rainstorm tracking algorithm: (a) IVT object identification and tracking; (b) Attached concurrent ERA5 precipitation and (c) AORC precipitation to identified IVT event. The top-left panel also shows the Mississippi River Basin, including the (1) Lower Mississippi, (2) Arkansas-Red, (3) Missouri, (4) Upper Mississippi, and (5) Ohio-Tennessee subbasins.

220

221 **3.2 Stochastic Rainfall Generator**

222 The Space-Time nOnstationary Rainfall Model for Large Area Basins (StormLab) was
223 developed based on ideas from Notaro et al. (2014) under a meta-Gaussian framework. For a
224 given ERA5/CESM2 rainstorm, 2D Gaussian noise was generated to represent precipitation
225 spatiotemporal structures and converted to precipitation amounts through parametric
226 distributions conditioned on large-scale atmospheric variables. Multiple noise realizations were
227 simulated to produce an ensemble of possible precipitation scenarios for each rainstorm event.
228 The model consists of three key components, described further below: 1) time-varying
229 precipitation distributions; 2) spatiotemporal noise generation; and 3) precipitation ensemble
230 simulation.

231 *3.2.1 Time-Varying Precipitation Distributions*

232 Parametric precipitation distributions conditioned on large-scale atmospheric variables were
233 modeled at each 0.03° grid cell. The distributions consist of two components:

234 1) A precipitation occurrence model that predicts the probability of precipitation
235 occurrence P_{wet} in a grid cell at time *t* using logistic regression (Sperandei, 2014):

236 $$P_{wet}(t) = \frac{1}{1+\exp(-[\alpha_0 + \alpha_1 PR_m(t) + \alpha_2 PW_m(t)])} \quad (1)$$

237 where PR_m and PW_m are ERA5/CESM2 precipitation and precipitable water linearly
238 interpolated to the grid, (i.e., the conditioned large-scale atmospheric variables). For model
239 fitting and validation, PR_m and PW_m were obtained from ERA5 rainstorms (see Section 3.3.1).
240 For model simulation, PR_m and PW_m were obtained from CESM2 rainstorms, under the
241 assumption that the statistical relationships derived from ERA5 and AORC hold for CESM2 (see
242 Section 3.3.2). α_0, α_1, and α_2 are fitted parameters.

243 2) A precipitation magnitude model that predicts the distribution of precipitation amount
244 in a "wet" grid cell using a transformed nonstationary gamma distribution (TNGD). Let *x*
245 represent the precipitation amount at a single grid point. We assumed *x* follows a generalized
246 gamma distribution with shape parameters $a > 0$, $c > 0$, and scale $b > 0$ (Stacy, 1962):

247 $$f_X(x,a,c,b) = \frac{c}{b\Gamma(a)}\left(\frac{x}{b}\right)^{ca-1}\exp\left(-\left(\frac{x}{b}\right)^{c}\right) \quad (2)$$

248 Applying a transformation $y = x^c$ gives $y \sim Gamma(a', b')$, where $a' = a$ and $b' = b^c$ (see
249 Supporting Information S3 for derivations):

$$f_Y(y, a', b') = \frac{1}{b'\Gamma(a')}\left(\frac{y}{b'}\right)^{a'-1}\exp\left(-\frac{y}{b'}\right) \quad (3)$$

The gamma distribution has mean $\mu = a'b'$ and variance $\sigma^2 = a'(b')^2$. To incorporate nonstationarity, the mean μ was modeled as a function of large-scale atmospheric variables (Scheuerer & Hamill, 2015):

$$\mu(t) = \frac{\mu_c}{\beta_0}\log\left\{1 + (\exp(\beta_0) - 1)\left[\beta_1 + \beta_2\frac{PR_m(t)}{\overline{PR}} + \beta_3\frac{PW_m(t)}{\overline{PW}}\right]\right\} \quad (4)$$

where μ_c is the mean of a stationary gamma distribution fitted to all the ERA5 rainstorms' AORC precipitation data at the grid, $\overline{PR}$ and $\overline{PW}$ are the climatological mean of ERA5 precipitation and precipitable water, $\beta_0, \beta_1, \beta_2$ and β_3 are fitted parameters. The variance σ^2 and shape parameter *c* were kept constant over time. The parameter *c* in the TNGD controls the tail heaviness of the distribution, allowing better fitting of extreme precipitation values compared to a basic gamma distribution. The transformation to variable *Y* also creates a simple relationship between the mean and distribution parameters that simplifies parameter estimation.

3.2.2 Spatiotemporal Noise Generation

We followed the STREAM (Hartke et al., 2022) approach, which itself is based heavily on Pysteps (Nerini et al., 2017; Pulkkinen et al., 2019), to simulate spatiotemporally correlated Gaussian noise that replicates the spatial and temporal dependency structure of the actual precipitation. Given an AORC precipitation field at the first time step t_0 of a rainstorm, we divided the field into overlapping spatial windows and computed the 2D Fourier amplitude spectrum within each window (Figure 2a). The amplitude spectra capture the spatial correlation of precipitation within each window while omitting phase information that determines the exact location of precipitation. For windows with less than 10% precipitation coverage, the global amplitude spectrum of the entire field was used.

Next, we filtered Gaussian white noise locally using the amplitude spectrum from each window:

$$n_{p_1,p_2} = FFT^{-1}\left\{|R_{p_1,p_2}| \circ \mathbf{N}\right\} \quad (5)$$

where n_{p_1,p_2} is the spatially correlated noise field, $|R_{p_1,p_2}|$ is the local amplitude spectrum for the window at the position (p_1, p_2), **N** is the Fourier Transform of uncorrelated Gaussian white noise, and $(\circ)$ is pointwise multiplication. This generates noise with local anisotropy and spatial dependence matching that of the original AORC precipitation within the window. The final nonstationary noise field is obtained by summing the local noise from all windows. We chose an empirical window size of (128, 128) grid cells to balance capturing localized precipitation structures and maintaining sufficient samples within each window. A 0.3 overlap ratio between windows was chosen to improve the smoothness of the final noise field. For any overlapping regions between windows, the noise values were averaged.

The correlated noise field at the next time step $t+1$ was modeled by a lag-1 autoregressive (AR(1)) model (Figure 2b):

$$n(t+1, i, j) = \rho n(t, i-v_t, j-u_t) + \sqrt{1-\rho^2}\, n(t+1, i, j) \quad (6)$$

where $n(t+1, i, j)$ is the noise value to be calculated at time $t+1$ and grid cell position (i, j), $n(t, i-v_t, j-u_t)$ is the noise value at time t, which means the noise is advected by the 850hPa north-south and east-west wind vector (v_t, u_t) from position $(i-v_t, j-u_t)$ at time t to position (i, j) at time $t+1$, $n(t+1, i, j)$ is the new spatially correlated noise generated at $t+1$, and ρ is the correlation coefficient between AORC precipitation at t and $t+1$.

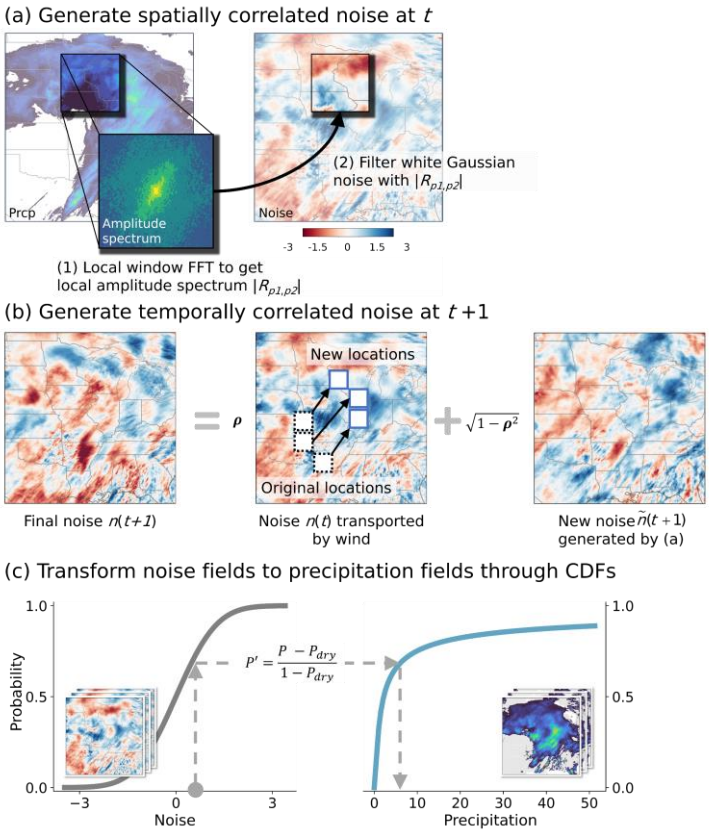

Figure 2. Process of spatiotemporal precipitation generation. (a) Generating spatially correlated noise using local window FFT based on high-resolution AORC precipitation; (b) Generating temporally correlated noise using the AR(1) model. ρ represents the correlation coefficient between precipitation fields at t and t+1; (c) Transforming noise fields to precipitation fields through CDFs.

Generating space-time correlated noise requires amplitude spectra from high-resolution AORC precipitation. For CESM2 rainstorms, corresponding high-resolution precipitation fields are not available. To obtain plausible spatial precipitation structures, we used a precipitation field matching method to find surrogate high-resolution precipitation fields from historical AORC

data (Figure 3). This matching assumes rainstorms with similar large-scale atmospheric conditions will exhibit similar precipitation patterns and spatial correlations. For each CESM2 time step, we computed the average Euclidean distance between the CESM2 atmospheric variable fields (precipitation, precipitable water, and IVT) and those from ERA5 rainstorms during 1979-2021:

$$d = \sqrt{\sum_{i=1}^{N}(PR_{ERA5,i} - PR_{CESM\,2,i})^2} + \sqrt{\sum_{i=1}^{N}(PW_{ERA5,i} - PW_{CESM\,2,i})^2} + \sqrt{\sum_{i=1}^{N}(IVT_{ERA5,i} - IVT_{CESM\,2,i})^2} \quad (7)$$

where N is the closest matching ERA5 time steps based on minimum Euclidean distance to the CESM2 time step. One of those five time steps was randomly sampled with a probability proportional to the inverse of the Euclidean distance. This ensures that ERA5 time steps with more similar atmospheric variables to the CESM2 time step have a higher probability of being sampled. The sampled time step provides an AORC precipitation field serving as the surrogate high-resolution precipitation, whose amplitude spectra are then used to generate spatially correlated noise. This matching is performed independently at each time step. In effect, this finds historical precipitation fields that resemble the spatial structure of a given CESM2 rainstorm. It only uses local and global amplitude spectra and discards the phase information, thus reducing effects from location mismatch between AORC and CESM2 precipitation. In rare cases when the local window with CESM2 precipitation contained no AORC data, the global amplitude spectrum of surrogate precipitation field was used as an approximation. Since the sampled AORC fields may lack temporal continuity, the correlation coefficient ρ in Equation 6 was computed based on CESM2 precipitation when simulating CESM2 rainstorms.

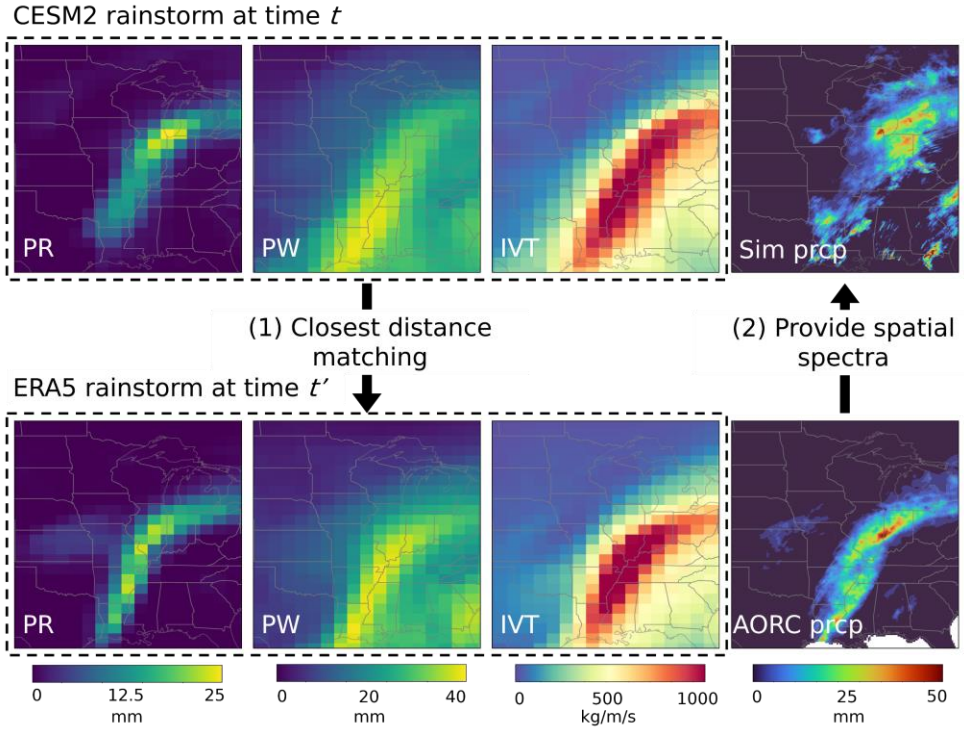

Figure 3. Process of precipitation field matching method. (1) Randomly selecting an ERA5 time step with the closest atmospheric variable fields to those at the target CESM2 time step; (2) Using AORC precipitation at the sampled ERA5 time step to provide local (high-resolution) amplitude spectra for the precipitation simulation at the target CESM2 time step.

3.2.3 Precipitation Ensemble Simulation

The actual precipitation field was obtained by transforming the noise field through the time-varying parametric precipitation distributions described in Section 3.2.1 (Figure 2c). The correlated noise field was first converted to a probability field using the CDF of the standard Gaussian distribution. If the transformed probability $P(t)$ at one grid is lower than the current dry probability $P_{dry}(t) = 1 - P_{wet}(t)$, the simulated precipitation was set to zero. If $P(t)$ exceeded $P_{dry}(t)$, the excess was rescaled to 0-1 as $P'(t) = \frac{P(t) - P_{dry}(t)}{1 - P_{dry}(t)}$. This $P'(t)$ was then converted to $y(t)$ using the inverse CDF of the fitted nonstationary Gamma distribution (Equation 3). The final precipitation $x(t)$ was calculated as $x(t) = y(t)^{1/c}$. Multiple correlated noise realizations for a rainstorm can be transformed to generate an ensemble of precipitation realizations. Each realization represents a possible precipitation scenario consistent with the current large-scale atmospheric state.

3.3 Experimental Design

An overview of the model experiments is as follows: The SRG was first fitted based on AORC precipitation and ERA5 large-scale atmospheric variables and then cross-validated (Section 3.3.1). Then, the SRG was used to simulate precipitation fields based on large-scale atmospheric variables from CESM2 rainstorms (Section 3.3.2). This assumes that the ERA5 and bias-corrected CESM2 rainstorms share similar characteristics, such that the established ERA5-AORC relationships can be applied to downscale CESM2 storms.

3.3.1 Model Fitting and Evaluation

The precipitation occurrence and magnitude models were fitted for each month from December-May using ERA5 rainstorms for 1979-2021. Fitting was performed at each 0.03° grid in the study domain (29-50°N, 79-113°W), consisting of 1024 × 630 grids. 6-hour AORC precipitation data and associated large-scale atmospheric variables (ERA5 precipitation and precipitable water) were extracted from the identified rainstorms. For logistic regression, AORC data were converted to 0 (dry) or 1 (wet) using a 0.2 mm threshold. The Python Scikit-learn package (Pedregosa et al., 2011) was used to estimate the logistic regression parameters using maximum likelihood. For TNGD, samples with AORC precipitation > 0.2 mm were first fitted to a stationary generalized gamma model using Scipy's method of moments (Virtanen et al., 2020). The estimated shape parameter *c* transformed the precipitation data as $y = x^c$. The new variable *y* was then fitted to the nonstationary gamma distribution (Equation 3). The distribution

parameters were estimated by minimizing the mean continuous ranked probability score (CRPS, units in mm, see Hersbach, 2000) using the optimization function in Scipy:

$$\frac{1}{n}\sum_{t=1}^{n} CRPS(F_t, y_t) \tag{8}$$

$$CRPS(F_t, y_t) = \int_{-\infty}^{+\infty} \left[F_t(z) - \mathbf{1}\left(y_t \le z\right) \right]^2 dz \tag{9}$$

where F_t is the CDF of nonstationary gamma distribution at time *t*, y_t is the transformed AORC precipitation, *n* is the sample size, and $\mathbf{1}\left(y_t \le z\right)$ is a Heaviside step function, which is 1 if $y_t \le z$ and 0 otherwise. CRPS measures the distance between CDFs, so minimizing the mean CRPS minimizes the difference between the parametric and empirical CDFs of observations at the grid.

We used five-fold cross-validation to evaluate out-of-sample model performance. The original 43 years of data were split into five folds. Each fold used 80% of the data for fitting and 20% for simulation and validation. To simulate an ERA5-based rainstorm, we first generated correlated noise fields based on AORC precipitation. The noise fields were converted to precipitation through the precipitation distributions conditioned on ERA5 large-scale atmospheric variables. We simulated 20 realizations per rainstorm, representing possible precipitation patterns other than the AORC precipitation. Looping through the five folds generated out-of-sample simulations for all ERA5 rainstorms. Key rainstorm characteristics, including total precipitation, rainstorm area, and space-time autocorrelation, were compared between simulations and AORC data. The Brier Score (BS) was used to assess the accuracy of predicted precipitation occurrence (wet or dry) at each grid (Benedetti, 2010):

$$BS(x_t, x_t) = \frac{1}{K}\sum_{i=1}^{K} \left[\mathbf{1}(x_{t,k} > 0) - \mathbf{1}(x_t > 0) \right]^2 \tag{10}$$

where *K* is the number of realizations, $x_{t,k}$ is the *k*th simulated precipitation at time *t*, and x_t is the AORC precipitation. BS ranges from 0 to 1, with 0 for perfect accuracy and 1 for highly inaccurate predictions. We also computed the Reduction CRPS as $RCRPS(F_t, x_t) = CRPS(F_t, x_t) / \sigma_0$ to assess the accuracy of simulated precipitation distribution at each grid cell (Trinh et al., 2013), where F_t is the empirical CDF of the 20 precipitation realizations at time *t* and σ_0 is the climatological standard deviation of the AORC precipitation. Compared to the original CRPS, RCRPS is normalized and thus independent of the precipitation magnitude at each grid, allowing spatial comparison of model performance across grids and subbasins. A lower value of RCRPS indicates a smaller difference between the CDFs of simulated and AORC precipitation.

390 *3.3.2 CESM2-based Rainstorm Simulations*

391 Random precipitation fields were generated for storms identified from ten CESM2 ensemble
392 members. For a given event, surrogate high-resolution precipitation fields were sampled using
393 the matching method described above (Section 3.2.2). Correlated noise was then generated and
394 transformed to precipitation based on the precipitation distributions conditioning on CESM2
395 large-scale atmospheric variables. To reduce computation, we simulated a single realization for
396 each rainstorm in the ten 100-year members. The resulting storm total precipitation distributions
397 were then compared against ERA5 rainstorm total precipitation accumulations. To estimate
398 extreme precipitation frequency, we selected simulated annual maxima rainstorms and generated
399 20 additional realizations for each event. Bootstrap resampling was implemented to estimate
400 return levels of annual maxima: 1) In each bootstrap sample, we randomly resampled 1,000 years
401 with replacement and selected one of the 20 annual maxima realizations for each year. 2) The
402 empirical CDF of annual maximum precipitation was obtained from this bootstrap sample. 3)
403 Steps 1 and 2 were repeated 5,000 times to estimate mean return levels and their uncertainties.

404

405 # 4 Results

406 ## 4.1 ERA5 and CESM2 Rainstorm Identification

407 The STARCH method identified intense IVT events and associated rainstorms over the basin
408 (e.g., Figures 1, 4a-c, and 11a-c). The tracked IVT objects exhibited an elongated, narrow
409 structure, with IVT intensities gradually decreasing from the center toward the edge. In most
410 cases, only one IVT object was present at a time, moving steadily from southwest to northeast
411 across the basin. Extensive precipitation associated with fronts or extratropical cyclones was
412 found near the high IVT regions, showing a clear link between strong water vapor transport and
413 heavy precipitation in the basin. Good agreement was found between ERA5 precipitation
414 patterns and AORC data, suggesting that ERA5 simulates realistic large-scale atmospheric
415 environments in which the rainstorms occurred. However, precipitation locations and spatial
416 distributions still differed at local scales, suggesting that local precipitation is partly determined
417 by mesoscale or finer-scale processes that are not fully resolved by ERA5 or CESM2.

418 Similar rainstorm characteristics were found between the 1,088 rainstorms identified from the
419 43-year ERA5 data and the 26,166 rainstorms from the 1,000-year bias-corrected CESM2 data
420 (Figure 5). The average annual number of rainstorms from December-May was 25 in ERA5 and
421 26 in CESM2 (Figure 5a). Average storm duration was around 50 hours for both datasets, with
422 maximum durations reaching 240 hours in ERA5 and 300 hours in CESM2 (Figure 5b). The
423 average precipitation area over the basin was about 1.3 million km^2, approximately 40% of the
424 basin area (Figure 5c). The average precipitation rate of the CESM2 rainstorms was 0.8% lower
425 than that of the ERA5 rainstorms, while average precipitable water and IVT were 4.3% and 3.5%
426 higher (Figures 5d-f). However, CESM2 rainstorms had a larger standard deviation in average
427 precipitation rate (18% higher) and lower standard deviations in average precipitable water and
428 IVT (5.2% and 5.9% lower). CESM2 rainstorms also exhibited more extreme values, with the
429 largest average precipitation rate of 10.6 mm/6-hour compared to 7 mm/6-hour in ERA5
430 rainstorms, likely due to its larger sample size and the inclusion of future climate projections.

Overall, bias-corrected CESM2 data produced rainstorms generally consistent with those from the ERA5 data, allowing them to be used for precipitation simulations. However, more complex biases may still exist in the CESM2 data after correction which can introduce some uncertainty into the simulated results.

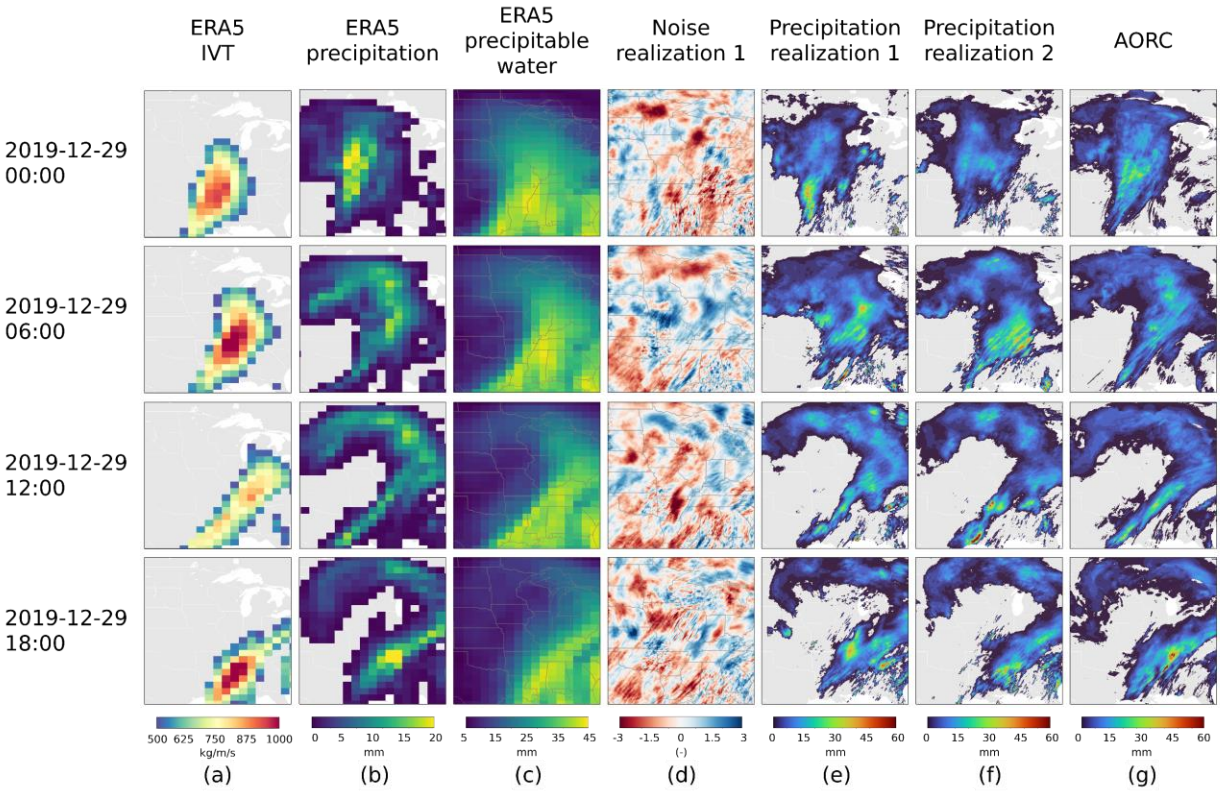

Figure 4. Spatiotemporal patterns of an ERA5-based rainstorm starting at 00:00 UTC on 29 December 2019. (a) ERA5 IVT; (b) ERA5 precipitation; (c) ERA5 precipitable water; (d) The first realization of noise; (e) The first realization of simulated precipitation; (f) The second realization of simulated precipitation; (g) Reference AORC precipitation.

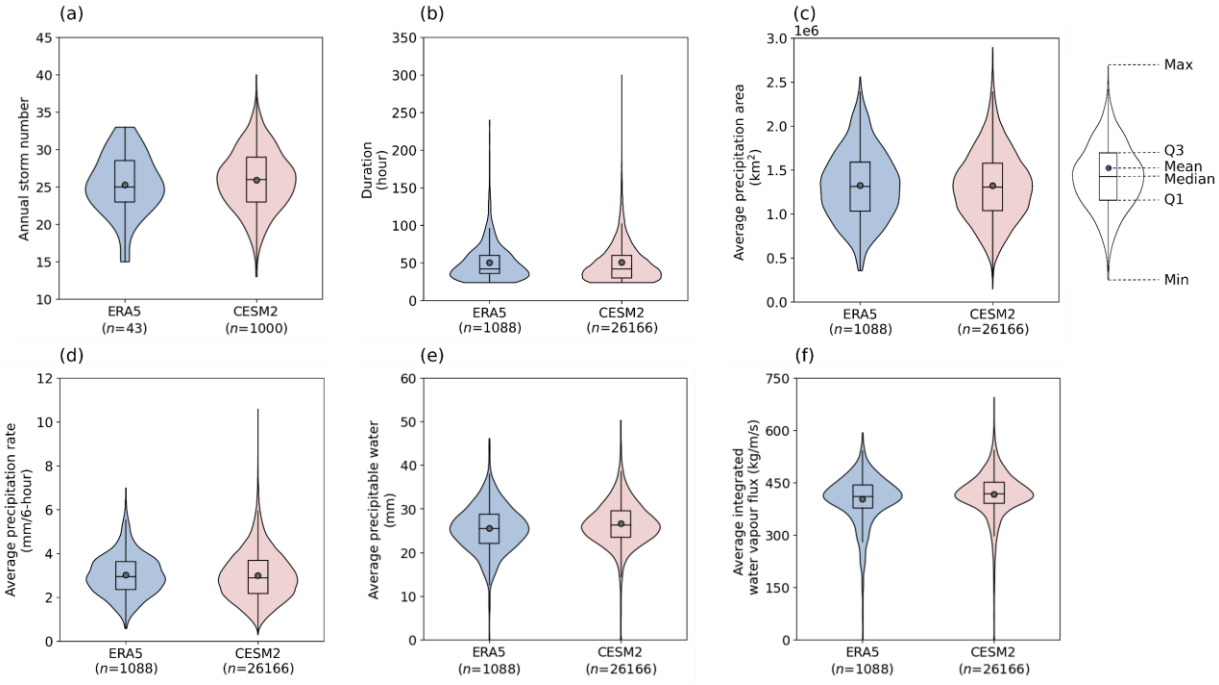

Figure 5. Distributions of rainstorm characteristics from ERA5 (blue) and CESM2 (red). (a) Annual storm number from Dec-May; (b) Storm duration; (c) Average precipitation area; (d) Average precipitation rate; (e) Average precipitable water; (f) Average integrated water vapor flux. *n* is the total number of identified rainstorms.

4.2 ERA5-based Rainstorm Simulation

This section evaluated the model performance by examining ERA5-based simulated rainstorms. Figure 4 shows a rainstorm in December 2019, with typical atmospheric conditions conducive to heavy precipitation: an extratropical cyclone system with intense IVT and high precipitable water covering the basin (Figures 4a-c). The Gaussian noise field captured local spatial structures of the AORC precipitation (Figure 4d). For example, the upper-left noise was smooth and continuous in the first time step, while the lower-right was fragmented, consistent with the AORC precipitation pattern (Figure 4g). The simulated spatiotemporal precipitation patterns were similar to the AORC data, exhibiting a comma-like structure (Figure 4e-g). The model simulated heavy precipitation in the regions of high ERA5 precipitation and precipitable water, showing positive relationships between the mean of precipitation distributions and large-scale atmospheric variables. Notably, however, the local patterns and hotspots of simulated precipitation differed from the AORC and varied across realizations, reflecting the stochasticity in small-scale precipitation processes that could occur under the same large-scale atmospheric conditions.

The simulated and AORC total precipitation fields for three extreme rainstorms preceding the 1997, 2011, and 2018 Mississippi Floods are shown in Figure 6. The rainstorms exhibited similar spatial orientations and coverage, with intense precipitation concentrated over the Lower Mississippi and Ohio-Tennessee subbasins. The simulated precipitation patterns and amounts generally agreed with the AORC data. For instance, total precipitation realizations for the 2018

event ranged from 47-57 mm with a mean of 51 mm, close to the 50 mm amount from AORC. Intense precipitation locations and shapes, however, differed from the AORC precipitation since the simulations were intended to represent multiple possible extreme scenarios. The AORC precipitation displayed stronger anisotropy and long-range spatial dependence (e.g., the more elongated arc of intense precipitation in the 1997 event, Figure 6b). Also, the AORC precipitation exhibited more continuous spatial variations, while the simulations contained more fragmented, noise-like textures. This suggests some discrepancies remained between the simulated and AORC precipitation structures that were not fully captured by the rainfall generator.

Consistency also existed in the temporal evolution of total precipitation, with the SRG ensemble spread (i.e., min to max) containing most of the AORC time series (Figure 7). Notably, the SRG ensemble mean only represents the general trend of simulations and does not necessarily match the AORC data. This is because the AORC precipitation is also a single realization of an underlying random process, and therefore may not always locate at the mean at every time point. The spatial autocorrelation functions (ACF) of simulated rainstorms were generally consistent with the AORC data, though slightly lower from 0-400 km (Figures 8a-b). The rainstorms exhibited short-term dependence, with temporal ACF dropping below 0.2 after the 12-hour lag (Figure 8c), supporting the AR(1) temporal noise model. The lag-1 ACF coefficients matched the AORC, except being lower for the 2018 event. The spatiotemporal patterns, precipitation time series, and ACFs were also examined for the remaining ERA5 rainstorms, yielding similar agreement.

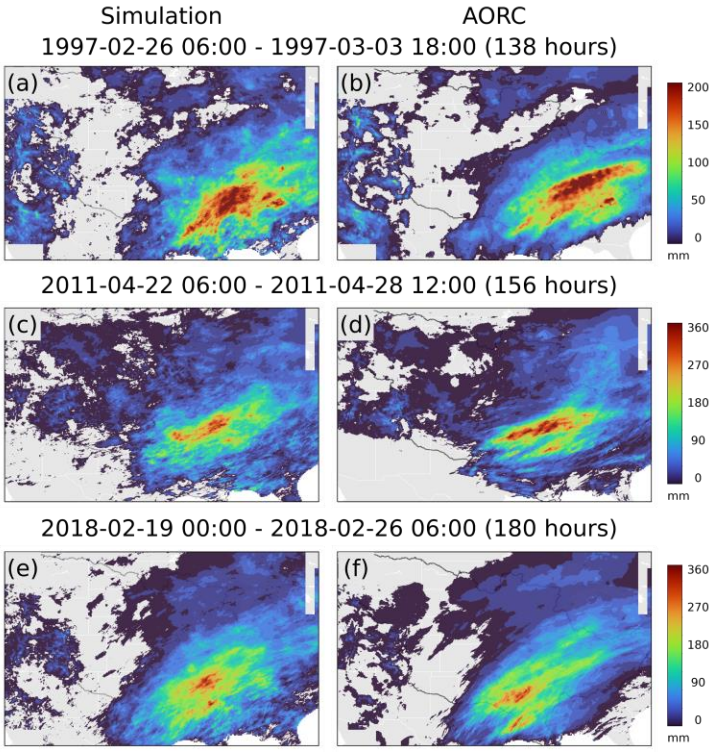

Figure 6. Total precipitation patterns from simulations (single realization) and AORC for rainstorms in (a-b) February 1997, (c-d) April 2011, and (e-f) February 2018.

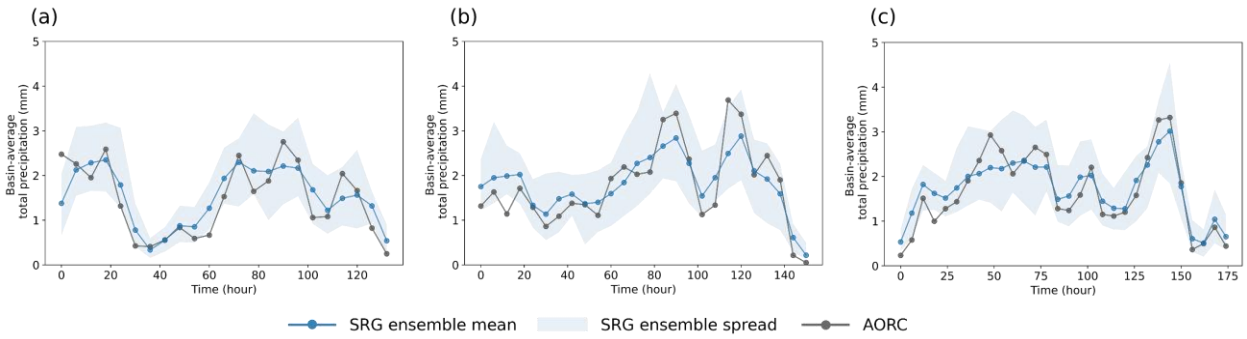

Figure 7. Time series of basin-average total precipitation from simulations (blue) and AORC (grey) for rainstorms in (a) February 1997, (b) April 2011, and (c) February 2018.

Basin-average total precipitation and rainstorm areas were compared between SRG ensemble mean and AORC for each rainstorm. Despite the model generating variant spatiotemporal patterns across realizations, the average total precipitation was highly correlated with the AORC data (correlation ρ = 0.97, Figure 9a). This consistency is partly because the time-varying precipitation distributions were conditioned on ERA5 large-scale atmospheric variables, which indirectly limits the range of possible precipitation values. Another explanation stems from the atmospheric water balance: the net water vapor flux entering the river basin—governed by large-scale atmospheric variables—should balance the total precipitation during an event, thus constraining possible precipitation amounts. There was also agreement in total and intense (>20 mm) precipitation areas between simulations and reference (ρ = 0.90 and 0.96, Figures 9b-c). For smaller rainstorms under 1.5 million km^2, however, the model tended to overestimate total precipitation area. This overestimation may result from the coarse ERA5 data not fully resolving the AORC precipitation patterns and overpredicting precipitation occurrence in some cases. Figure 1b at 18 hours, for example, illustrated an example where ERA5 generated greater precipitation coverage than the AORC data.

Model performance was also evaluated at each grid cell using the Brier Score and RCRPS. The average BS over the basin was 0.11, suggesting good accuracy in simulating precipitation occurrence (Figure 10a). Comparatively higher BS was seen in the Ohio-Tennessee (an average of 0.14), Lower Mississippi (0.13), and Upper Mississippi (0.12) subbasins (Figure 10b). The average RCRPS was 0.18 over the basin, indicating satisfactory agreement between simulated and AORC precipitation distributions (Figure 10c). The Ohio-Tennessee subbasin had the highest average RCRPS of 0.25, followed by 0.22 in the Lower Mississippi and 0.2 in the Upper Mississippi subbasins (Figure 10d). The BS and RCRPS patterns suggest higher SRG uncertainties in regions experiencing more extreme and frequent rainstorms. A potential explanation is that these regions exhibit more complex precipitation processes, e.g., localized convection or orographic lift, leading to more uncertain relationships between large-scale atmospheric environments and local precipitation.

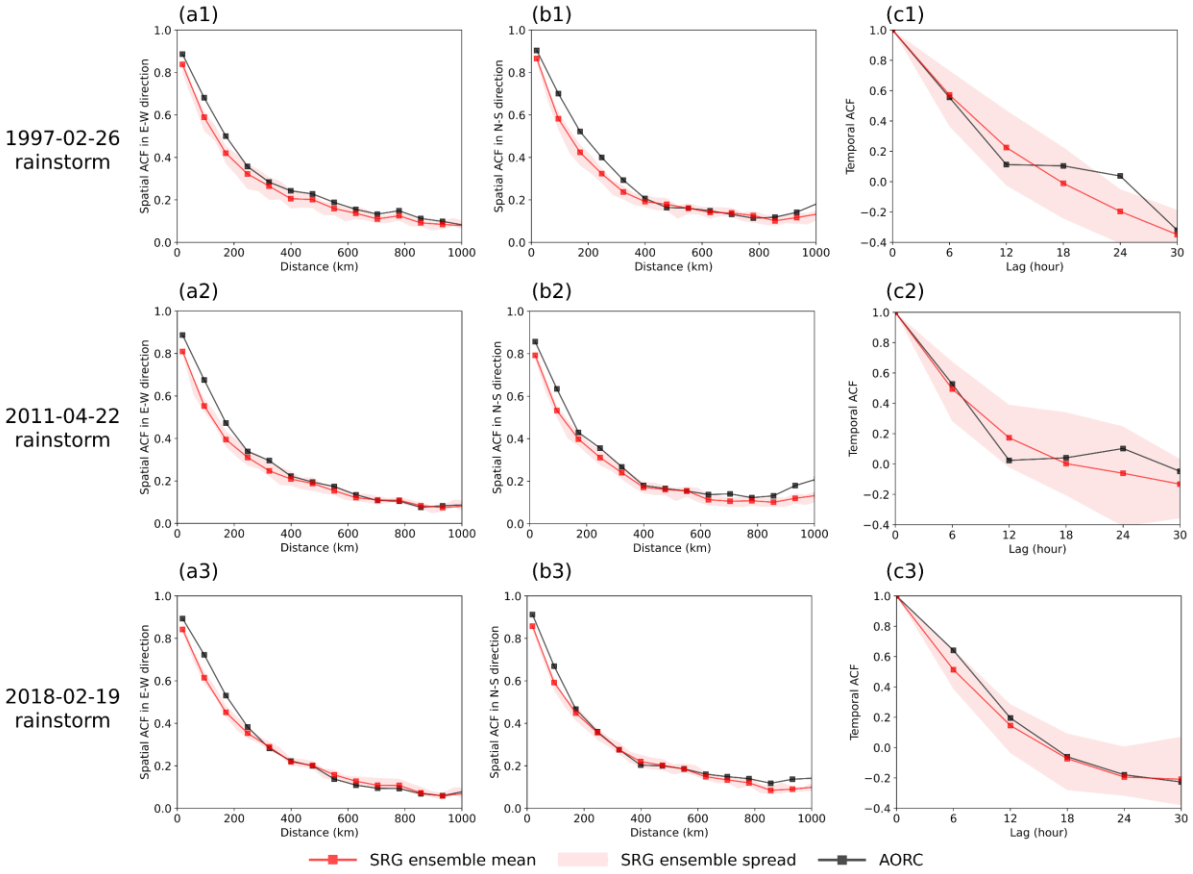

Figure 8. Comparison of spatiotemporal ACFs between simulations (red) and AORC data (black) for rainstorms in February 1997, April 2011, and February 2018. (a1-3) Average spatial ACF in East-West direction; (b1-3) Average spatial ACF in North-South direction; (c1-3) temporal ACF of basin-average total precipitation.

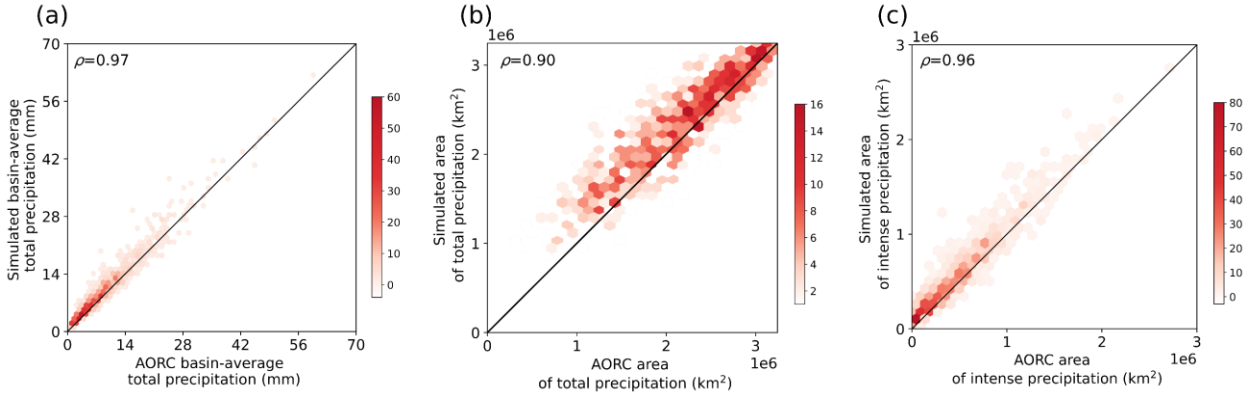

Figure 9. Comparison of rainstorm characteristics between SRG ensemble mean and AORC for each ERA5 rainstorm. (a) Basin-average total precipitation; (b) Total precipitation area; (c) Total intense precipitation area (>20 mm).

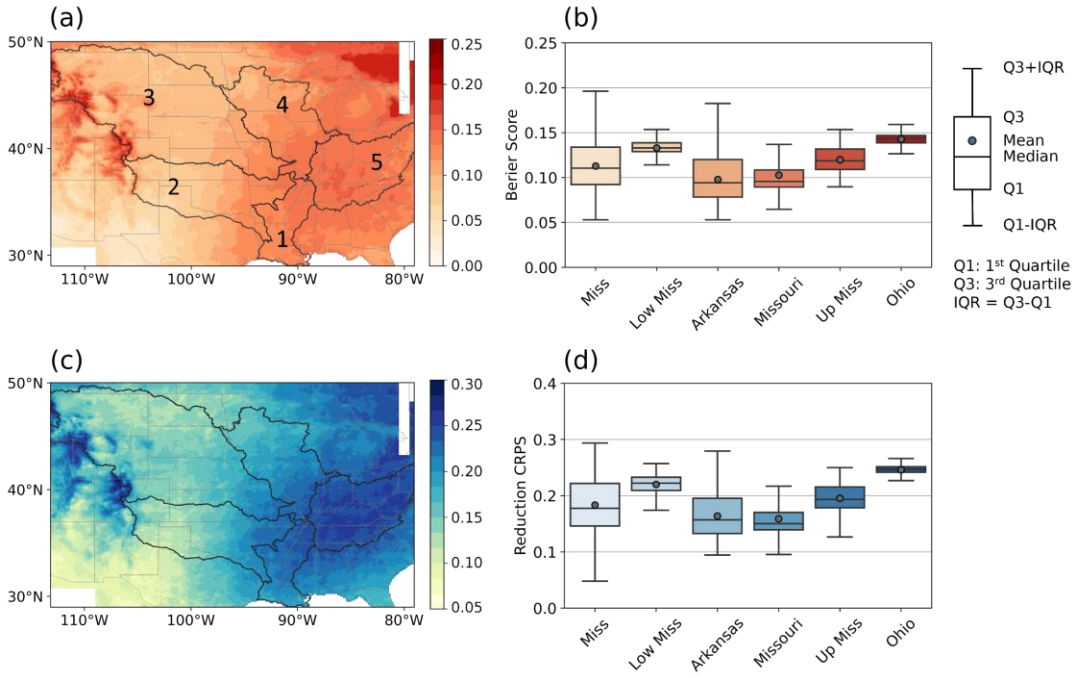

Figure 10. (a) Brier Scores across the simulation domain; (b) Boxplots of Brier Scores in the Mississippi River Basin and the five subbasins; (c) Reduction CRPSs across the simulation domain; (d) Boxplots of Reduction CRPSs in the Mississippi River Basin and the five subbasins. The five subbasins are also shown in (a), including (1) Lower Mississippi, (2) Arkansas-Red, (3) Missouri, (4) Upper Mississippi, and (5) Ohio-Tennessee subbasins.

4.3 CESM2-based Rainstorm Simulation

Spatiotemporal patterns of a CESM2 rainstorm in March 2022 are shown in Figure 11. The matched AORC precipitation, despite being sampled from different time steps, exhibited similar locations and shapes to the CESM2 precipitation, providing reasonable approximations of precipitation spatial structures. The simulated precipitation fields more closely resembled the CESM2 patterns rather than the sampled AORC fields. This is because precipitation occurrence and magnitude are mainly determined by precipitation distributions conditioned on CESM2 large-scale atmospheric variables, while only the spatial correlation was drawn from the AORC data. The SRG realizations had very similar precipitation coverage and shape, with differences primarily in intense precipitation locations. This indicates the SRG ensemble members are not fully independent due to their shared reliance on the same large-scale atmospheric conditions.

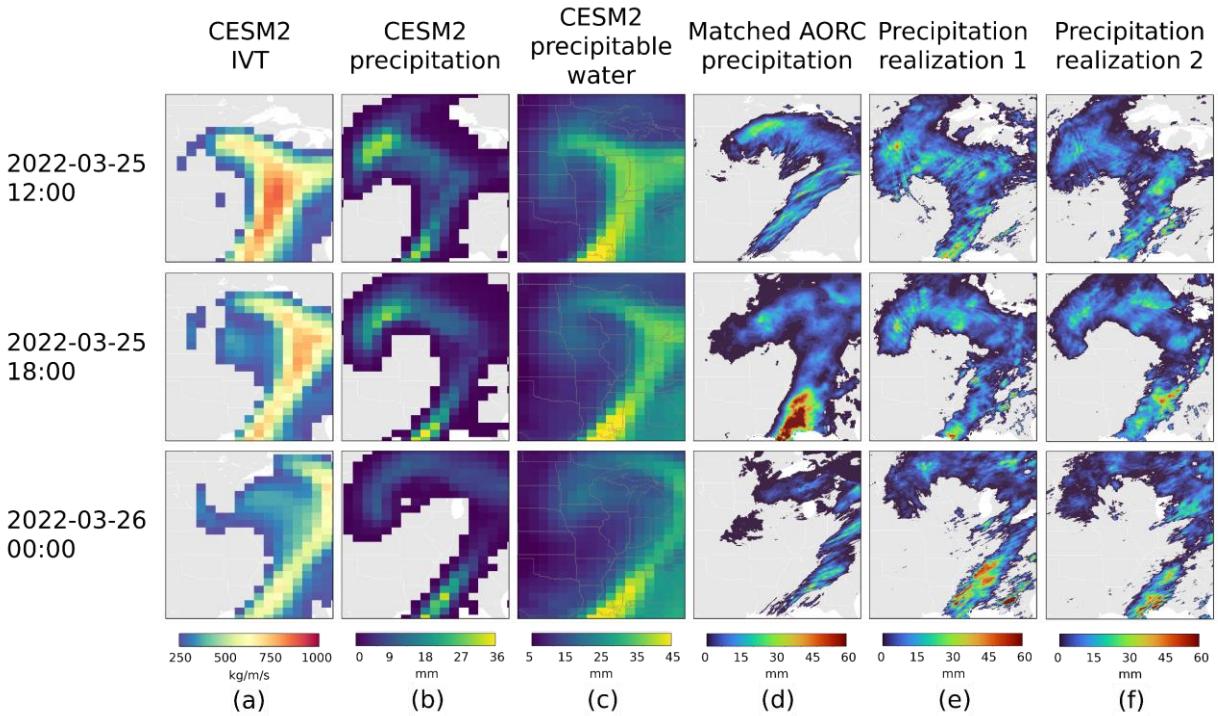

Figure 11. Spatiotemporal patterns of a CESM2-based rainstorm starting at 12:00 UTC on 25 March 2022. (a) CESM2 IVT; (b) CSEM2 precipitation; (c) CSEM2 precipitable water; (d) Matched AORC historical precipitation at 2020-03-29 00:00, 1983-04-14 06:00, and 2019-03-15 00:00, respectively; (e) The first realization of simulated precipitation; (f) The second realization of simulated precipitation. The date does not mean this CESM2 rainstorm happened historically, as it is generated from CESM2 simulations representing various atmospheric states under historical forcing.

One realization of simulated total precipitation and associated atmospheric variables for three extreme rainstorms are shown in Figure 12. The events produced basin-average precipitation of 67, 75, and 91 mm, roughly equivalent to 50-year, 100-year, and 1,000-year events based on the GEV distribution fitted to the reference data (GEV fitting shown in Figure 15). All three rainstorms occurred in early spring and were characterized by long-lived (>160 hours) strong water vapor transport from the Gulf of Mexico. Consistent with ERA5 rainstorms, the simulated precipitation patterns exhibited southwest-northeast orientations, with intense precipitation near high CESM2 precipitation and precipitable water. The 1,000-year event displayed the greatest area of heavy precipitation (>300 mm), covering nearly the entire Lower Mississippi and parts of adjacent subbasins. Multiple peaks occurred in the simulated precipitation series (Figure 13), which is also an evident trait in ERA5 rainstorms (Figure 7). Despite showing similar trends to the original CESM2 precipitation, SRG ensemble members showed greater variability in temporal precipitation series. This enhanced variability in the SRG ensembles is more evident in the total precipitation amounts. For example, the total precipitation produced by the SRG ranged from 79-99 mm for the April 1962 event, whereas the bias-corrected CESM2 data showed 78 mm (Figure 13c). This suggests that the SRG introduces variability not only in the spatiotemporal precipitation patterns but also in the total precipitation amount of a rainstorm

event. This randomness could potentially cover more extreme scenarios and lead to important variability in flood responses.

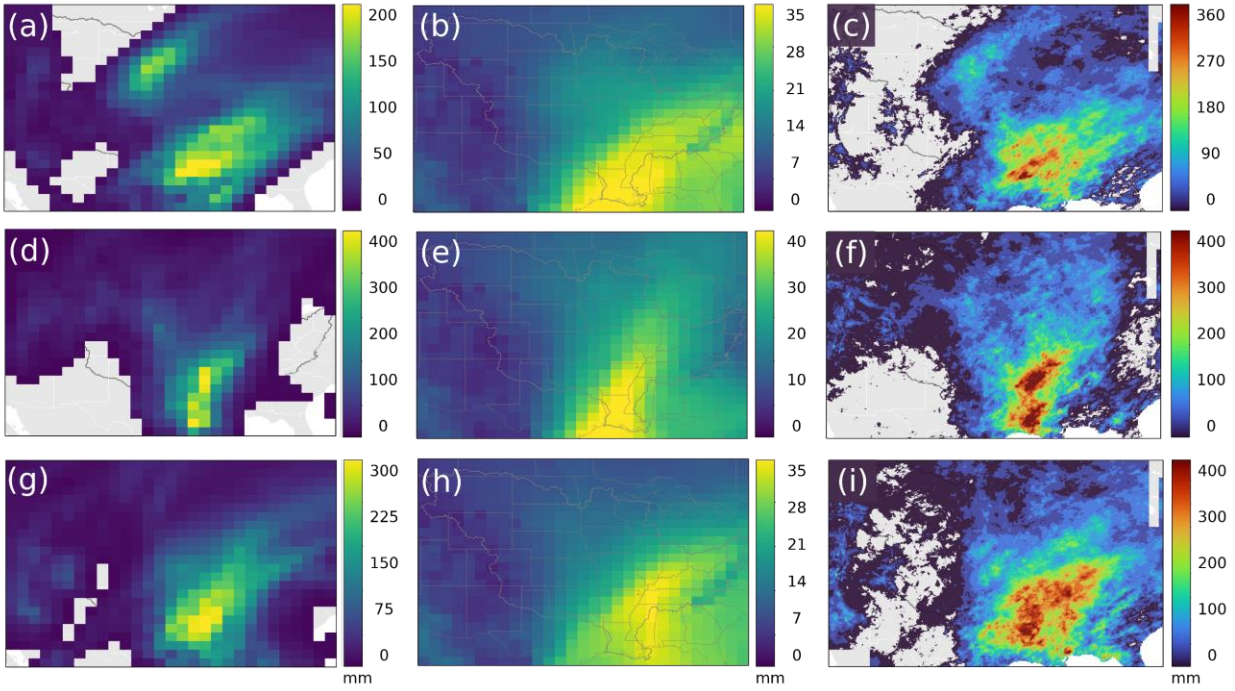

Figure 12. Total CESM2 precipitation (a, d, g), average CESM2 precipitable water (b, e, h), and total simulated precipitation (c, f, i) of CESM2 rainstorms in March 2022 (162 hours), April 2029 (162 hours), and April 1962 (264 hours).

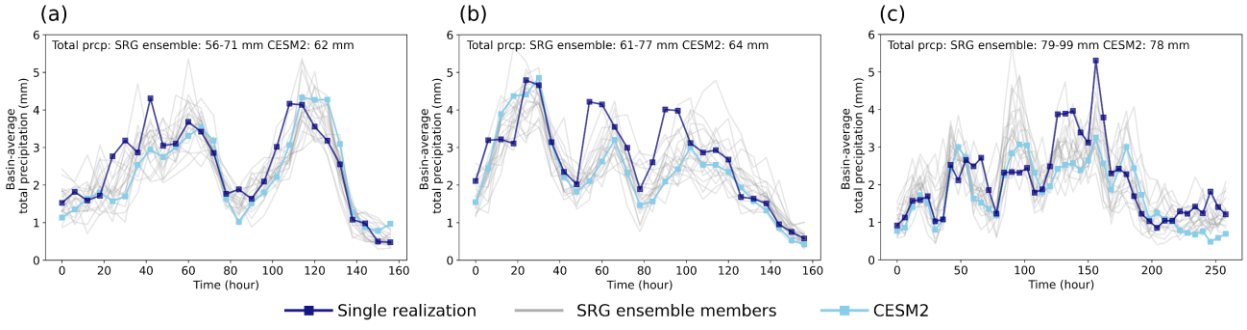

Figure 13. Time series of basin-average total precipitation of CESM2 rainstorms in (a) March 2022, (b) April 2029, and (c) April 1962. The dark blue line represents the rainstorm realization shown in Figure 12, and the grey lines represent the 20 SRG ensemble members. The light blue line represents the bias-corrected CESM2 data.

The simulated total precipitation distributions of all CESM2 rainstorms (26,166 events) generally agreed with the AORC data for each month (Figure 14). An exception was May, where the

model tended to simulate more events with 5-10 mm total precipitation. The L-kurtosis, a measure of tail heaviness based on L-moments (T. J. Smith et al., 2023), was computed for each month using 1,000 bootstraps (Table 1). The average L-kurtosis was 0.161 for the simulations and 0.167 for the AORC, suggesting similar tail behavior. However, the simulations exhibited significantly lighter tails (lower L-kurtosis) in December and heavier tails (higher L-kurtosis) in May, likely resulting from remaining biases in CESM2 data.

Table 1. L-kurtosis of total precipitation distributions.

Month	Dec	Jan	Feb	Mar	Apr	May	Avg
CESM2 rainstorms	0.147	0.156	0.154	0.159	0.153	0.196	0.161
AORC	0.218	0.138	0.175	0.155	0.166	0.151	0.167

The return levels of annual maximum total precipitation from the CESM2-based simulations agreed well with the AORC data (Figure 15). In contrast, the original bias-corrected CESM2 data significantly underestimated the extreme precipitation, indicating it may not be suitable for directly representing extreme scenarios. For comparison, a GEV distribution was also fitted to the reference annual maxima using L-moments (T. J. Smith et al., 2023). The simulation-based estimates were slightly higher than the GEV for 10-500 year recurrence intervals, staying closer to the AORC precipitation points. However, beyond 500 years, the estimates increased slower than the GEV, yielding a lower 1,000-year return level of 89 mm. This likely results from the GEV exhibiting a heavy, unbounded tail (shape parameter = 0.1), while the SRG simulations seem to be bounded. The bounded tail implies a maximum possible event in the basin, which is physically reasonable because the precipitation was constrained by large-scale atmospheric variables and space-time correlation structures. Also, the GEV tail behavior can be highly uncertain due to fitting difficulty given the limited sample size. The tail heaviness of extreme precipitation has been investigated and discussed by many studies (e.g., National Research Council, 1994; Koutsoyiannis, 2004; Papalexiou & Koutsoyiannis, 2013; Francesco Serinaldi & Kilsby, 2014; Marani & Ignaccolo, 2015). It is widely recognized that commonly-used extreme value distributions (including GEV) may not adequately represent the underlying precipitation processes, causing high certainties at the tails. To address this, the SRG may help investigate tail behavior based on large-sample simulations. Our results suggest the extreme precipitation driven by strong IVT is bounded in the Mississippi River Basin.

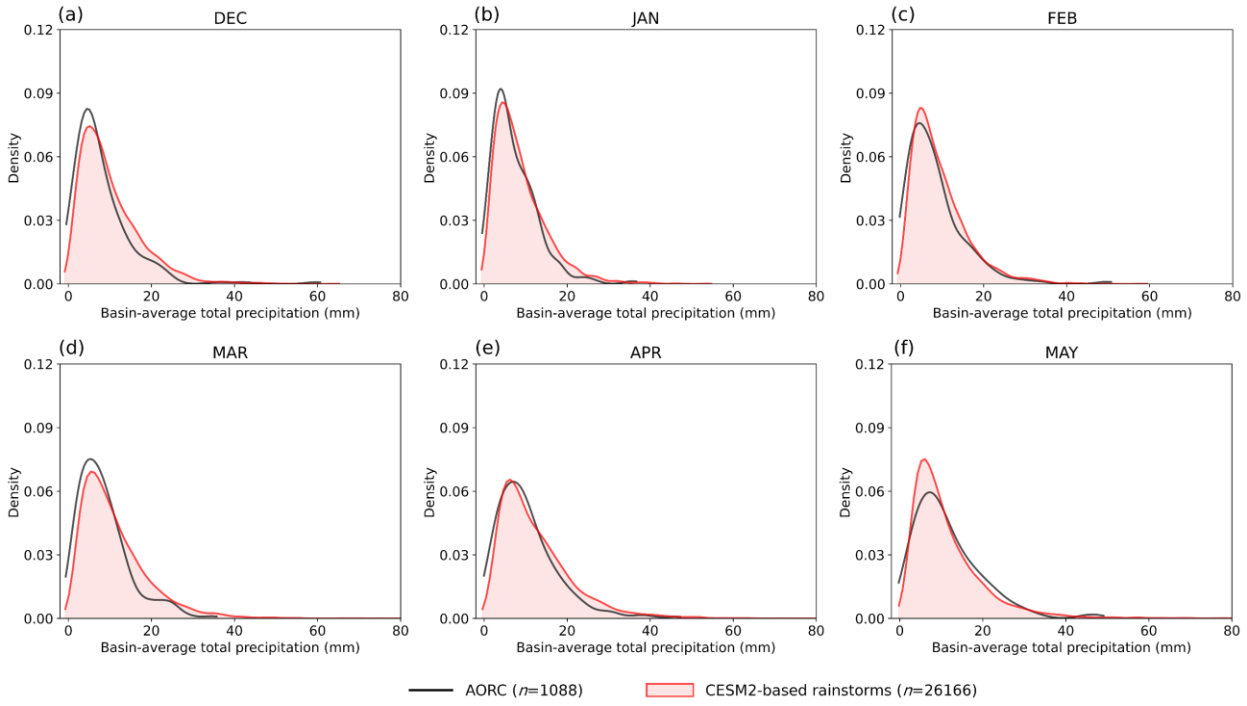

615

616 Figure 14. Distributions of basin-average total precipitation between simulated CESM2
617 rainstorms (red) and AORC (black) from December-May. *n* is the total number of rainstorms.

618

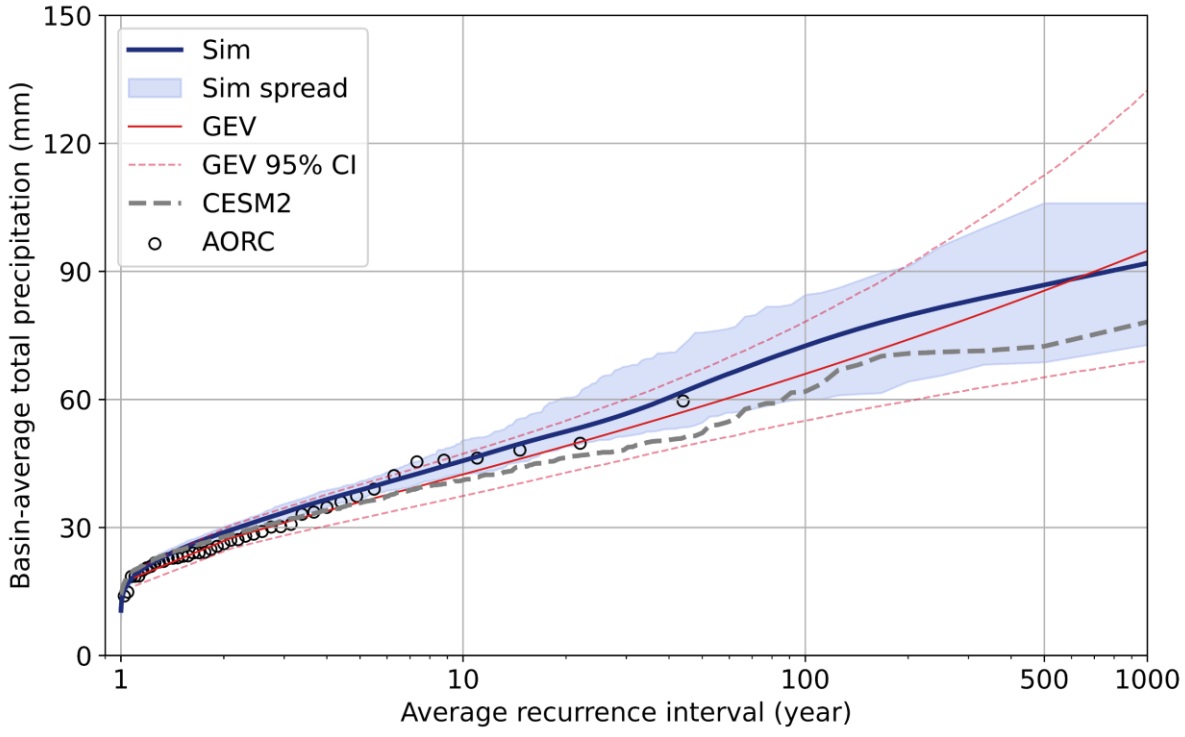

619

Figure 15. Comparison of estimated return levels of annual maximum precipitation based on stochastic simulations conditioned on CESM2 rainstorms (blue line) and the GEV distribution (red line). Dashed gray line represents the original bias-corrected CESM2 precipitation.

5. Discussion

5.1 Contribution to Design Flood in the lower Mississippi River Basin

The simulations from our SRG potentially contribute to the design flood in MRB by extending the choice of historical rainstorms to over 1,000 synthetic years of events based on CESM2 data. The design flood study of V. A. Myers (1959) revealed that it is a critical sequence of extreme rainstorms—as opposed to a single precipitation event—that is likely to cause the most extreme flood in the lower MRB (Su et al., 2023). In other words, the flood magnitude depends on storm arrival orders in the MRB and time of concentration—flood discharge due to downstream precipitation can be amplified by peak discharges coming from upstream rainstorms. While developing new hypothetical storm sequences is beyond the scope of this study, we highlight that rainstorm sequences can be determined directly based on their arrivals in CESM2 simulations, providing a large number of more physically reasonable sequences compared to "manual creation" of one (as in Hypo-Flood 58A) or several sequences. Note that a rainstorm sequence with 1,000-year total precipitation does not necessarily result in a flood with 1,000-year peak discharge—because flood responses are determined by many other factors, including watershed antecedent conditions, spatiotemporal precipitation patterns, and arrival locations of rainstorms. Therefore, future work will be to integrate the precipitation simulations with large-scale hydrologic models to analyze peak discharge outputs and identify rainstorm sequences that result in floods at certain average recurrence intervals.

5.2 Model Uncertainty

Multiple sources of uncertainties exist in the model that can influence the simulation results. This section discusses three major sources of uncertainty: 1) uncertainty from data sources; 2) uncertainty from precipitation distributions; and 3) uncertainty from precipitation spatiotemporal structures.

5.2.1 Uncertainty from Data Sources

Biases in datasets contributed to model uncertainties in different ways. The AORC data, created by downscaling daily NLDAS-2 and Stage IV precipitation, may not fully capture the extreme precipitation values at hourly scales, introducing bias when fitting precipitation distributions and extracting precipitation spatial correlation structures. Meanwhile, although ERA5 is corrected by extensive observations via data assimilation, biases in large-scale atmospheric variables can be higher in earlier periods (e.g., before 2000) due to fewer available observational data. A key source of uncertainty arises from the way in which ERA5 and CESM2 data are used—while the rainfall generator was fitted based on AORC precipitation and ERA5 large-scale atmospheric variables, CESM2 data were used as covariates to simulate rainstorms, assuming the fitted statistical relationships can be transferred to CESM2. Though bias correction of CESM2 was used to reduce its biases relative to ERA5, this could not eliminate discrepancies in spatial and temporal correlation structures. For instance, CESM2 tends to generate smoother precipitation

patterns and larger areas of intense IVT and precipitable water than ERA5. To reduce this uncertainty, more advanced bias correction methods could be applied to correct temporal and spatial structures of CESM2 data (e.g., Cannon, 2018; Mathieu Vrac & Thao, 2020; Robin & Vrac, 2021). However, one must be careful, as such multi-aspect bias corrections may damage or lose information in the original CESM2 data, such as climate change signals.

5.2.2 Uncertainty from Precipitation Distributions

The logistic regression model achieved good prediction accuracy in precipitation occurrence (see Brier Scores in Figure 10), although spatial variations existed across sub-basins. Greater uncertainties originated from fitting the TNGD due to its more complicated structure and larger number of parameters. Compared to simply fitting a Gamma distribution, TNGD improved tail fitting with the transformation parameter c. However, some grids still exhibited under- or overestimation of extreme precipitation. The transformed variable y was assumed to have a distribution mean being a non-linear function of large-scale atmospheric variables and a constant standard deviation, which simplified climate change influences as precipitation variance may increase in the future. Also, while maximum precipitable water scales at approximately 7%/K following the Clausius-Clapeyron equation (Held & Soden, 2006), extreme precipitation generally does not follow the same scaling, depending on factors such as precipitation type, duration, and location (Lochbihler et al., 2017; X. Zhang et al., 2017; Fowler et al., 2021). This suggests that precipitable water, when used as the covariate, may increase faster than actual precipitation in future projections, resulting in overestimation of the distribution mean. A possible modification is to use an alternative covariate suggested by O'Gorman & Schneider (2009) that incorporates vertical velocity and moist-adiabatic lapse rate, which scales better with extreme precipitation under temperature changes.

5.2.3 Uncertainty from Precipitation Spatiotemporal Structures

While the SRG generated overall consistent rainstorm patterns and shapes as compared to the AORC precipitation, approximating precipitation structures using spatiotemporal Gaussian noise can introduce uncertainties in precipitation simulations. Although the local-window FFT improved representation of local precipitation spatial structures, it reduced samples in each window and decreased the accuracy of the frequency spectrum that is related to spatial correlation. Precipitation fields in the local windows were assumed to be stationary, which can neglect some highly localized, anisotropic precipitation processes like local convection and orographic effects. Cropping the precipitation field by window also lost precipitation long-range structural information, weakening long-range dependence in simulated precipitation (see Section 4.2). Non-linear transformation via precipitation distributions can reduce correlation strength between Gaussian noise (Papalexiou, 2022), which may explain the reduced spatial ACF of simulated rainstorms (see Section 4.2 and Figure 8). One possible improvement is applying a residual spectrum to the original amplitude spectrum as compensation for correlation loss during transformation. For the time dimension, the AR(1) model omitted precipitation temporal dependence beyond lag 2 and can also be influenced by the quality and resolution of 850 hPa wind data, introducing additional uncertainties.

Another key source of uncertainty came from the precipitation field matching method for CESM2 rainstorms. The sampled AORC precipitation—although sharing similar large-scale

atmospheric variable patterns—can have different spatial coverage and local precipitation structures to the unknown precipitation fields of CESM2 rainstorms. Also, independent sampling at each time step reduced temporal coherence of spatial structures, compared to ERA5 rainstorm simulations based on consecutive AORC fields. Since AORC data only covered 43 years, there might be no suitable AORC precipitation pattern for some CESM2 rainstorms. These uncertainties arose from the rainfall generator's reliance on high-resolution precipitation for spatial correlation information. To address this limitation, one potential solution is to use parametric spatial correlation models for each local window, with coefficients estimated based on current large-scale atmospheric variables. Another way is leveraging deep learning models like generative adversarial networks (e.g., pix2pix, Isola et al., 2017) or diffusion models (e.g., SR3, Saharia et al., 2022) to predict high-resolution precipitation or spectrum fields.

6 Summary and Conclusions

In the study, a stochastic rainfall generator StormLab was proposed to simulate 6-hour, 0.03° rainstorm fields driven by strong water vapor flux in the Mississippi River Basin. The model used a local-window FFT-based approach to simulate nonstationary Gaussian noise fields that capture local spatial structures and temporal evolution of precipitation. The noise fields were transformed into actual precipitation amounts through precipitation distributions at each grid cell, where precipitation occurrence was modeled with logistic regression, and precipitation magnitude was represented by a transformed nonstationary Gamma distribution (TNGD). The precipitation probability and mean of TNGD were modeled as functions of large-scale atmospheric variables (i.e., ERA5/CESM2 precipitation and precipitable water) to incorporate spatial and temporal nonstationarity. Given the large-scale atmospheric variable fields of a rainstorm, the model could simulate multiple precipitation realizations representing possible precipitation scenarios.

Spatiotemporal rainstorms driven by strong IVT were identified from 1979-2021 based on ERA5 reanalysis and high-resolution AORC precipitation using a rainstorm tracking method STARCH. Precipitation distributions were fitted monthly at each grid cell for December-May based on the identified rainstorms. To evaluate the model performance, key rainstorm characteristics were compared between StormLab simulations and reference data, including spatiotemporal patterns, total precipitation, precipitation area, and spatiotemporal ACFs, showing good consistency. The average Brier Score and Reduction CRPS were 0.11 and 0.18 over the basin, suggesting high precipitation occurrence accuracy and good agreement between simulated and AORC precipitation distributions. However, these metrics were higher in the Ohio-Tennessee, Lower, and Upper Mississippi River Basins, indicating greater model uncertainty in regions with more extreme precipitation.

The model generated 1,000 synthetic years of rainstorms based on events from 10 bias-corrected CESM2 ensemble simulations from 1950-2050. Since CESM2 lacks high-resolution precipitation data to extract spatial correlation structures, a matching algorithm was implemented to sample historical AORC fields for each CESM2 event. Empirical return levels of annual maximum precipitation from the simulations showed better agreement with the AORC data than the GEV distribution. In future work, the model simulations will provide extreme rainstorm samples to update the current design storm sequence in the lower Mississippi River Basin.

The proposed model overcomes limitations of existing SRGs by enabling nonstationary simulations for continental-scale river basins. By focusing on the key flood-generating mechanism (i.e., strong IVT), the model avoids the difficulty of representing multiple complex weather systems and precipitation processes. Notably, while this study focused on simulating winter and spring extreme rainstorms, the model can be extended for continuous, long-term simulations. Another advantage is that the model predicts precipitation distributions—rather than specific precipitation values—conditioned on large-scale atmospheric variables, followed by generating multiple noise and precipitation realizations. This reflects the concept that there are multiple possible local precipitation processes consistent with a given large-scale atmospheric state. Therefore, the model can also be viewed not only as a step forward in stochastic rainfall generation, but also as a novel stochastic downscaling approach to disaggregate coarse GCM outputs. Compared to the original CESM2 precipitation, the model is able to introduce variability not only in the spatiotemporal precipitation patterns but also in the total precipitation amounts. This suggests that conditioning on large-scale atmospheric variables can provide additional information to improve SGR simulations of storm arrivals, spatiotemporal structures, and precipitation distributions, particularly under a changing climate.

The model is not without limitations, however. One major shortcoming is its reliance on sufficient gridded precipitation and atmospheric variable data for fitting distributions and extracting precipitation spatial structures. Biases in the atmospheric variables will propagate through the fitted precipitation distributions and influence simulations. There are also uncertainties when using spatial correlation structures from historical AORC precipitation for CESM2 rainstorms. One way to improve the model is to use parametric spatial covariance models for local precipitation structures, with parameters inferred from large-scale atmospheric variable fields. Future work will integrate the model simulations with hydrologic models to study influences of rainstorm sequences on basin flooding. Another direction is applying the model to other weather systems like tropical cyclones that contribute to coastal floods and other extreme hazards.

Acknowledgments

The contributions of the authors were supported by the US National Science Foundation (NSF) Hydrologic Sciences Program (award number 1749638). The authors thank the Center for High Throughput Computing (CHTC) at the University of Wisconsin-Madison for providing computing sources and technical support. The authors thank Ruihai Wu for providing suggestions for obtaining space-time correlation structures from CESM2 data.

Data Availability Statement

AORC precipitation data can be downloaded from the National Oceanic Atmospheric Administration data storage website (https://hydrology.nws.noaa.gov/aorc-historic/). ERA5 Reanalysis data is available at the ECMWF Climate Data Store (https://doi.org/10.24381/cds.adbb2d47). CESM2 Large-Ensemble Project data is available from Climate Data Gateway at the National Center for Atmospheric Research

(https://www.earthsystemgrid.org/dataset/ucar.cgd.cesm2le.atm.proc.6hourly_ave.html). StormLab codes are available on GitHub (https://github.com/lorenliu13/StormLab). STREAM and STARCH codes are available on Zenodo (http://doi.org/10.5281/zenodo.6564982, Hartke, 2022, and https://doi.org/10.5281/zenodo.7091017, Y. Liu & Wright, 2022b). Other codes and data from this study are available from the authors upon request.

Conflict of Interest

The authors declare no conflicts of interest relevant to this study.

References

Ailliot, P., Allard, D., Monbet, V., & Naveau, P. (2015). Stochastic weather generators: an overview of weather type models. *Journal de La Société Française de Statistique*, *156*(1), 101--113.

Ban, N., Schmidli, J., & Schär, C. (2015). Heavy precipitation in a changing climate: Does short-term summer precipitation increase faster? *Geophysical Research Letters*, *42*(4), 1165–1172. https://doi.org/10.1002/2014GL062588

Barlow, M., Gutowski, W. J., Gyakum, J. R., Katz, R. W., Lim, Y.-K., Schumacher, R. S., et al. (2019). North American extreme precipitation events and related large-scale meteorological patterns: a review of statistical methods, dynamics, modeling, and trends. *Climate Dynamics*, *53*(11), 6835–6875. https://doi.org/10.1007/s00382-019-04958-z

803 Baxevani, A., & Lennartsson, J. (2015). A spatiotemporal precipitation generator based on a
804 censored latent Gaussian field. *Water Resources Research*, *51*(6), 4338–4358.
805 https://doi.org/10.1002/2014WR016455

806 Benedetti, R. (2010). Scoring Rules for Forecast Verification. *Monthly Weather Review*, *138*(1),
807 203–211. https://doi.org/10.1175/2009MWR2945.1

808 Benoit, L., Allard, D., & Mariethoz, G. (2018). Stochastic Rainfall Modeling at Sub-kilometer
809 Scale. *Water Resources Research*, *54*(6), 4108–4130.
810 https://doi.org/10.1029/2018WR022817

811 Budikova, D., Coleman, J. S. M., Strope, S. A., & Austin, A. (2010). Hydroclimatology of the
812 2008 Midwest floods. *Water Resources Research*, *46*(12).
813 https://doi.org/10.1029/2010WR009206

814 Burton, A., Fowler, H. J., Kilsby, C. G., & O'Connell, P. E. (2010). A stochastic model for the
815 spatial-temporal simulation of nonhomogeneous rainfall occurrence and amounts. *Water*
816 *Resources Research*, *46*(11). https://doi.org/10.1029/2009WR008884

817 Cannon, A. J. (2018). Multivariate quantile mapping bias correction: an N-dimensional
818 probability density function transform for climate model simulations of multiple
819 variables. *Climate Dynamics*, *50*(1), 31–49. https://doi.org/10.1007/s00382-017-3580-6

820 Chen, Y., Paschalis, A., Wang, L.-P., & Onof, C. (2021). Can we estimate flood frequency with
821 point-process spatial-temporal rainfall models? *Journal of Hydrology*, *600*, 126667.
822 https://doi.org/10.1016/j.jhydrol.2021.126667

Cowpertwait, P. S. P. (1995). A generalized spatial-temporal model of rainfall based on a clustered point process. *Proceedings of the Royal Society of London. Series A: Mathematical and Physical Sciences*, *450*(1938), 163–175. https://doi.org/10.1098/rspa.1995.0077

Danabasoglu, G., Lamarque, J.-F., Bacmeister, J., Bailey, D. A., DuVivier, A. K., Edwards, J., et al. (2020). The Community Earth System Model Version 2 (CESM2). *Journal of Advances in Modeling Earth Systems*, *12*(2), e2019MS001916. https://doi.org/10.1029/2019MS001916

Dirmeyer, P. A., & Brubaker, K. L. (1999). Contrasting evaporative moisture sources during the drought of 1988 and the flood of 1993. *Journal of Geophysical Research: Atmospheres*, *104*(D16), 19383–19397. https://doi.org/10.1029/1999JD900222

Dirmeyer, P. A., & Kinter III, J. L. (2009). The "Maya Express": Floods in the U.S. Midwest. *Eos, Transactions American Geophysical Union*, *90*(12), 101–102. https://doi.org/10.1029/2009EO120001

Fall, G., Kitzmiller, D., Pavlovic, S., Zhang, Z., Patrick, N., St. Laurent, M., et al. (2023). The Office of Water Prediction's Analysis of Record for Calibration, version 1.1: Dataset description and precipitation evaluation. *JAWRA Journal of the American Water Resources Association*. https://doi.org/10.1111/1752-1688.13143

Fischer, E. M., & Knutti, R. (2016). Observed heavy precipitation increase confirms theory and early models. *Nature Climate Change*, *6*(11), 986–991. https://doi.org/10.1038/nclimate3110

Fouedjio, F. (2017). Second-order non-stationary modeling approaches for univariate geostatistical data. *Stochastic Environmental Research and Risk Assessment*, *31*(8), 1887–1906. https://doi.org/10.1007/s00477-016-1274-y

Fouedjio, F., Desassis, N., & Rivoirard, J. (2016). A generalized convolution model and estimation for non-stationary random functions. *Spatial Statistics*, *16*, 35–52. https://doi.org/10.1016/j.spasta.2016.01.002

Foufoula-Georgiou, E., & Krajewski, W. (1995). Recent advances in rainfall modeling, estimation, and forecasting. *Reviews of Geophysics*, *33*(S2), 1125–1137. https://doi.org/10.1029/95RG00338

Fowler, H. J., Lenderink, G., Prein, A. F., Westra, S., Allan, R. P., Ban, N., et al. (2021). Anthropogenic intensification of short-duration rainfall extremes. *Nature Reviews Earth & Environment*, *2*(2), 107–122. https://doi.org/10.1038/s43017-020-00128-6

Fuglstad, G.-A., Simpson, D., Lindgren, F., & Rue, H. (2015). Does non-stationary spatial data always require non-stationary random fields? *Spatial Statistics*, *14*, 505–531. https://doi.org/10.1016/j.spasta.2015.10.001

Gaines, R., Girdner, S., & Frederick, B. (2019). *Mississippi River and Tributaries flowline assessment hydrology report*. Engineer Research and Development Center (U.S.). https://doi.org/10.21079/11681/32693

Gori, A., Lin, N., Xi, D., & Emanuel, K. (2022). Tropical cyclone climatology change greatly exacerbates US extreme rainfall–surge hazard. *Nature Climate Change*, 1–8. https://doi.org/10.1038/s41558-021-01272-7

865 Gupta, V. K., & Waymire, E. C. (1993). A Statistical Analysis of Mesoscale Rainfall as a
866 Random Cascade. *Journal of Applied Meteorology and Climatology*, *32*(2), 251–267.
867 https://doi.org/10.1175/1520-0450(1993)032<0251:ASAOMR>2.0.CO;2

868 Hartke, S. H., Wright, D. B., Li, Z., Maggioni, V., Kirschbaum, D. B., & Khan, S. (2022).
869 Ensemble Representation of Satellite Precipitation Uncertainty Using a Nonstationary,
870 Anisotropic Autocorrelation Model. *Water Resources Research*, *58*(8), e2021WR031650.
871 https://doi.org/10.1029/2021WR031650

872 Held, I. M., & Soden, B. J. (2006). Robust Responses of the Hydrological Cycle to Global
873 Warming. *Journal of Climate*, *19*(21), 5686–5699. https://doi.org/10.1175/JCLI3990.1

874 Hersbach, H. (2000). Decomposition of the Continuous Ranked Probability Score for Ensemble
875 Prediction Systems. *Weather and Forecasting*, *15*(5), 559–570.
876 https://doi.org/10.1175/1520-0434(2000)015<0559:DOTCRP>2.0.CO;2

877 Hersbach, H., Bell, B., Berrisford, P., Biavati, G., Horányi, A., Muñoz Sabater, J., et al. (2018).
878 ERA5 hourly data on single levels from 1979 to present. *Copernicus Climate Change*
879 *Service (C3S) Climate Data Store (CDS)*, *10*.

880 Hitchens, N. M., Brooks, H. E., & Schumacher, R. S. (2013). Spatial and Temporal
881 Characteristics of Heavy Hourly Rainfall in the United States. *Monthly Weather Review*,
882 *141*(12), 4564–4575. https://doi.org/10.1175/MWR-D-12-00297.1

883 Hristopulos, D. T. (2020). *Random fields for spatial data modeling: a primer for scientists and*
884 *engineers*. Dordrecht, The Netherlands: Springer. https://doi.org/10.1007/978-94-024-
885 1918-4

886 Isola, P., Zhu, J.-Y., Zhou, T., & Efros, A. A. (2017). Image-to-image translation with
887 conditional adversarial networks. In *Proceedings of the IEEE conference on computer*
888 *vision and pattern recognition* (pp. 1125–1134).

889 Jothityangkoon, C., Sivapalan, M., & Viney, N. R. (2000). Tests of a space-time model of daily
890 rainfall in southwestern Australia based on nonhomogeneous random cascades. *Water*
891 *Resources Research*, *36*(1), 267–284. https://doi.org/10.1029/1999WR900253

892 Kaczmarska, J., Isham, V., & Onof, C. (2014). Point process models for fine-resolution rainfall.
893 *Hydrological Sciences Journal*, *59*(11), 1972–1991.
894 https://doi.org/10.1080/02626667.2014.925558

895 Koutsoyiannis, D. (2004). Statistics of extremes and estimation of extreme rainfall: II. Empirical
896 investigation of long rainfall records / Statistiques de valeurs extrêmes et estimation de
897 précipitations extrêmes: II. Recherche empirique sur de longues séries de précipitations.
898 *Hydrological Sciences Journal*, *49*(4), null-610.
899 https://doi.org/10.1623/hysj.49.4.591.54424

900 Lavers, D. A., & Villarini, G. (2013). Atmospheric Rivers and Flooding over the Central United
901 States. *Journal of Climate*, *26*(20), 7829–7836. https://doi.org/10.1175/JCLI-D-13-
902 00212.1

903 Le Cam, L. (1961). A STOCHASTIC DESCRIPTION OF PRECIPITATION. In J. Neyman
904 (Ed.), *Contributions to Astronomy, Meteorology, and Physics* (pp. 165–186). University
905 of California Press. https://doi.org/10.1525/9780520323438-010

Leblois, E., & Creutin, J.-D. (2013). Space-time simulation of intermittent rainfall with prescribed advection field: Adaptation of the turning band method. *Water Resources Research*, *49*(6), 3375–3387. https://doi.org/10.1002/wrcr.20190

Leinonen, J., Nerini, D., & Berne, A. (2021). Stochastic Super-Resolution for Downscaling Time-Evolving Atmospheric Fields With a Generative Adversarial Network. *IEEE Transactions on Geoscience and Remote Sensing*, *59*(9), 7211–7223. https://doi.org/10.1109/TGRS.2020.3032790

Leonard, M., Lambert, M. F., Metcalfe, A. V., & Cowpertwait, P. S. P. (2008). A space-time Neyman–Scott rainfall model with defined storm extent. *Water Resources Research*, *44*(9). https://doi.org/10.1029/2007WR006110

Lewis, J., McKinnie, C., Parrish, K., Crosby, W., Cruz, C., Dove, M., et al. (2019). *Mississippi River and Tributaries flowline assessment main report* (No. 24). United States. Army. Corps of Engineers. Mississippi Valley Division. https://doi.org/10.21079/11681/32623

Liu, B., Tan, X., Gan, T. Y., Chen, X., Lin, K., Lu, M., & Liu, Z. (2020). Global atmospheric moisture transport associated with precipitation extremes: Mechanisms and climate change impacts. *WIREs Water*, *7*(2), e1412. https://doi.org/10.1002/wat2.1412

Liu, Y., & Wright, D. (2022a, September 18). lorenliu13/starch: STARCH (Storm Tracking And Regional CHaracterization) (Version v1.0.1). Zenodo. https://doi.org/10.5281/ZENODO.7091017

925 Liu, Y., & Wright, D. B. (2022b). A storm-centered multivariate modeling of extreme
926 precipitation frequency based on atmospheric water balance. *Hydrology and Earth*
927 *System Sciences*, *26*(20), 5241–5267. https://doi.org/10.5194/hess-26-5241-2022

928 Lochbihler, K., Lenderink, G., & Siebesma, A. P. (2017). The spatial extent of rainfall events
929 and its relation to precipitation scaling. *Geophysical Research Letters*, *44*(16).
930 https://doi.org/10.1002/2017gl074857

931 Marani, M., & Ignaccolo, M. (2015). A metastatistical approach to rainfall extremes. *Advances*
932 *in Water Resources*, *79*, 121–126. https://doi.org/10.1016/j.advwatres.2015.03.001

933 Marra, F., Armon, M., & Morin, E. (2022). Coastal and orographic effects on extreme
934 precipitation revealed by weather radar observations. *Hydrology and Earth System*
935 *Sciences*, *26*(5), 1439–1458. https://doi.org/10.5194/hess-26-1439-2022

936 Marsan, D., Schertzer, D., & Lovejoy, S. (1996). Causal space-time multifractal processes:
937 Predictability and forecasting of rain fields. *Journal of Geophysical Research:*
938 *Atmospheres*, *101*(D21), 26333–26346. https://doi.org/10.1029/96JD01840

939 Mascaro, G., Papalexiou, S. M., & Wright, D. B. (2023). Advancing Characterization and
940 Modeling of Space-Time Correlation Structure and Marginal Distribution of Short-
941 Duration Precipitation. *Advances in Water Resources*, *177*, 104451.
942 https://doi.org/10.1016/j.advwatres.2023.104451

943 Matte, D., Christensen, J. H., & Ozturk, T. (2021). Spatial extent of precipitation events: when
944 big is getting bigger. *Climate Dynamics*. https://doi.org/10.1007/s00382-021-05998-0

McWilliams, C. D., & Hayes, G. W. (2017). Comparison of the 2011 Mississippi River Flood to the MR-T Project Design Flood. *Journal of Hydrologic Engineering*, *22*(5), E5015002. https://doi.org/10.1061/(ASCE)HE.1943-5584.0001238

Mehrotra, R., Srikanthan, R., & Sharma, A. (2006). A comparison of three stochastic multi-site precipitation occurrence generators. *Journal of Hydrology*, *331*(1), 280–292. https://doi.org/10.1016/j.jhydrol.2006.05.016

Menabde, M., Harris, D., Seed, A., Austin, G., & Stow, D. (1997). Multiscaling properties of rainfall and bounded random cascades. *Water Resources Research, 33*(12), 2823–2830.

Moore, B. J., Neiman, P. J., Ralph, F. M., & Barthold, F. E. (2012). Physical Processes Associated with Heavy Flooding Rainfall in Nashville, Tennessee, and Vicinity during 1–2 May 2010: The Role of an Atmospheric River and Mesoscale Convective Systems. *Monthly Weather Review*, *140*(2), 358–378. https://doi.org/10.1175/MWR-D-11-00126.1

Mutel, C. F. (Ed.). (2010). *A watershed year: anatomy of the Iowa floods of 2008*. Iowa City: University of Iowa Press.

Myers, M. F., & White, G. F. (1993). The Challenge of the Mississippi Flood. *Environment: Science and Policy for Sustainable Development*, *35*(10), 6–35. https://doi.org/10.1080/00139157.1993.9929131

Myers, V. A. (1959). Meteorology of Hypothetical Flood Sequences in the Mississippi River Basin. U.S. Department of Commerce Weather Bureau.

National Research Council. (1994). *Estimating Bounds on Extreme Precipitation Events: A Brief Assessment*. Washington : National Academies Press. https://doi.org/10.17226/9195

Nerini, D., Besic, N., Sideris, I., Germann, U., & Foresti, L. (2017). A non-stationary stochastic ensemble generator for radar rainfall fields based on the short-space Fourier transform. *Hydrology and Earth System Sciences*, *21*(6), 2777–2797. https://doi.org/10.5194/hess-21-2777-2017

Niemi, T. J., Kokkonen, T., & Seed, A. W. (2014). A simple and effective method for quantifying spatial anisotropy of time series of precipitation fields. *Water Resources Research*, *50*(7), 5906–5925. https://doi.org/10.1002/2013WR015190

Northrop, P. (1998). A clustered spatial-temporal model of rainfall. *Proceedings of the Royal Society A: Mathematical, Physical and Engineering Sciences*, *454*(1975), 1875–1888. https://doi.org/10.1098/rspa.1998.0238

Notaro, M., Lorenz, D., Hoving, C., & Schummer, M. (2014). Twenty-First-Century Projections of Snowfall and Winter Severity across Central-Eastern North America. *Journal of Climate*, *27*(17), 6526–6550. https://doi.org/10.1175/JCLI-D-13-00520.1

O'Gorman, P. A., & Schneider, T. (2009). The physical basis for increases in precipitation extremes in simulations of 21st-century climate change. *Proceedings of the National Academy of Sciences*, *106*(35), 14773–14777. https://doi.org/10.1073/pnas.0907610106

Onof, C., & Wang, L.-P. (2020). Modelling rainfall with a Bartlett–Lewis process: new developments. *Hydrology and Earth System Sciences*, *24*(5), 2791–2815. https://doi.org/10.5194/hess-24-2791-2020

985 Over, T. M., & Gupta, V. K. (1996). A space-time theory of mesoscale rainfall using random
986 cascades. *Journal of Geophysical Research: Atmospheres*, *101*(D21), 26319–26331.
987 https://doi.org/10.1029/96JD02033

988 Pan, Z., Zhang, Y., Liu, X., & Gao, Z. (2016). Current and future precipitation extremes over
989 Mississippi and Yangtze River basins as simulated in CMIP5 models. *Journal of Earth*
990 *Science*, *27*(1), 22–36. https://doi.org/10.1007/s12583-016-0627-2

991 Papalexiou, S. M. (2018). Unified theory for stochastic modelling of hydroclimatic processes:
992 Preserving marginal distributions, correlation structures, and intermittency. *Advances in*
993 *Water Resources*, *115*, 234–252. https://doi.org/10.1016/j.advwatres.2018.02.013

994 Papalexiou, S. M. (2022). Rainfall Generation Revisited: Introducing CoSMoS-2s and
995 Advancing Copula-Based Intermittent Time Series Modeling. *Water Resources Research*,
996 *58*(6), e2021WR031641. https://doi.org/10.1029/2021WR031641

997 Papalexiou, S. M., & Koutsoyiannis, D. (2013). Battle of extreme value distributions: A global
998 survey on extreme daily rainfall. *Water Resources Research*, *49*(1), 187–201.
999 https://doi.org/10.1029/2012WR012557

1000 Papalexiou, S. M., & Serinaldi, F. (2020). Random Fields Simplified: Preserving Marginal
1001 Distributions, Correlations, and Intermittency, With Applications From Rainfall to
1002 Humidity. *Water Resources Research*, *56*(2), e2019WR026331.
1003 https://doi.org/10.1029/2019WR026331

1004 Papalexiou, S. M., Serinaldi, F., & Porcu, E. (2021). Advancing Space-Time Simulation of
1005 Random Fields: From Storms to Cyclones and Beyond. *Water Resources Research*,
1006 *57*(8), e2020WR029466. https://doi.org/10.1029/2020WR029466

1007 Paschalis, A., Molnar, P., Fatichi, S., & Burlando, P. (2013). A stochastic model for high-
1008 resolution space-time precipitation simulation. *Water Resources Research*, *49*(12), 8400–
1009 8417. https://doi.org/10.1002/2013WR014437

1010 Pedregosa, F., Varoquaux, G., Gramfort, A., Michel, V., Thirion, B., Grisel, O., et al. (2011).
1011 Scikit-learn: Machine learning in Python. *Journal of Machine Learning Research*, *12*,
1012 2825–2830.

1013 Pulkkinen, S., Nerini, D., Pérez Hortal, A. A., Velasco-Forero, C., Seed, A., Germann, U., &
1014 Foresti, L. (2019). Pysteps: an open-source Python library for probabilistic precipitation
1015 nowcasting (v1.0). *Geoscientific Model Development*, *12*(10), 4185–4219.
1016 https://doi.org/10.5194/gmd-12-4185-2019

1017 Qin, J. (2011). *A High-Resolution Hierarchical Model for Space-Time Rainfall*. University of
1018 Newcastle.

1019 Rampal, N., Gibson, P. B., Sood, A., Stuart, S., Fauchereau, N. C., Brandolino, C., et al. (2022).
1020 High-resolution downscaling with interpretable deep learning: Rainfall extremes over
1021 New Zealand. *Weather and Climate Extremes*, *38*, 100525.
1022 https://doi.org/10.1016/j.wace.2022.100525

1023 Raut, B. A., Seed, A. W., Reeder, M. J., & Jakob, C. (2018). A Multiplicative Cascade Model for
1024 High-Resolution Space-Time Downscaling of Rainfall. *Journal of Geophysical*
1025 *Research: Atmospheres*, *123*(4), 2050–2067. https://doi.org/10.1002/2017JD027148

1026 Raut, B. A., Reeder, M. J., Jakob, C., & Seed, A. W. (2019). Stochastic Space-Time
1027 Downscaling of Rainfall Using Event-Based Multiplicative Cascade Simulations. *Journal*
1028 *of Geophysical Research: Atmospheres*, *124*(7), 3889–3902.
1029 https://doi.org/10.1029/2018JD029343

1030 Robin, Y., & Vrac, M. (2021). Is time a variable like the others in multivariate statistical
1031 downscaling and bias correction? *Earth System Dynamics*, *12*(4), 1253–1273.
1032 https://doi.org/10.5194/esd-12-1253-2021

1033 Rodgers, K. B., Lee, S.-S., Rosenbloom, N., Timmermann, A., Danabasoglu, G., Deser, C., et al.
1034 (2021). Ubiquity of human-induced changes in climate variability. *Earth System*
1035 *Dynamics*, *12*(4), 1393–1411. https://doi.org/10.5194/esd-12-1393-2021

1036 Rodriguez-Iturbe, I., Cox, D. R., & Isham, V. (1997). Some models for rainfall based on
1037 stochastic point processes. *Proceedings of the Royal Society of London. A. Mathematical*
1038 *and Physical Sciences*, *410*(1839), 269–288. https://doi.org/10.1098/rspa.1987.0039

1039 Rupp, D. E., Licznar, P., Adamowski, W., & Leśniewski, M. (2012). Multiplicative cascade
1040 models for fine spatial downscaling of rainfall: parameterization with rain gauge data.
1041 *Hydrology and Earth System Sciences*, *16*(3), 671–684. https://doi.org/10.5194/hess-16-
1042 671-2012

1043 Saharia, C., Ho, J., Chan, W., Salimans, T., Fleet, D. J., & Norouzi, M. (2022). Image super-
1044 resolution via iterative refinement. *IEEE Transactions on Pattern Analysis and Machine*
1045 *Intelligence*, *45*(4), 4713–4726.

1046 Sam Hartke. (2022). sam-hartke/STREAM: STREAMv1.0 (Version 1.0). Zenodo.
1047 https://doi.org/10.5281/zenodo.6564982

1048 Schertzer, D., & Lovejoy, S. (1987). Physical modeling and analysis of rain and clouds by
1049 anisotropic scaling multiplicative processes. *Journal of Geophysical Research:*
1050 *Atmospheres*, *92*(D8), 9693–9714. https://doi.org/10.1029/JD092iD08p09693

1051 Scheuerer, M., & Hamill, T. M. (2015). Statistical Postprocessing of Ensemble Precipitation
1052 Forecasts by Fitting Censored, Shifted Gamma Distributions*. *Monthly Weather Review*,
1053 *143*(11), 4578–4596. https://doi.org/10.1175/MWR-D-15-0061.1

1054 Schleiss, M., Chamoun, S., & Berne, A. (2014). Nonstationarity in Intermittent Rainfall: The
1055 "Dry Drift." *Journal of Hydrometeorology*, *15*(3), 1189–1204.
1056 https://doi.org/10.1175/JHM-D-13-095.1

1057 Schumacher, R. S., & Rasmussen, K. L. (2020). The formation, character and changing nature of
1058 mesoscale convective systems. *Nature Reviews Earth & Environment*, *1*(6), 300–314.
1059 https://doi.org/10.1038/s43017-020-0057-7

1060 Seed, A. W., Pierce, C. E., & Norman, K. (2013). Formulation and evaluation of a scale
1061 decomposition-based stochastic precipitation nowcast scheme. *Water Resources*
1062 *Research*, *49*(10), 6624–6641. https://doi.org/10.1002/wrcr.20536

1063 Serinaldi, F. (2010). Multifractality, imperfect scaling and hydrological properties of rainfall
1064 time series simulated by continuous universal multifractal and discrete random cascade
1065 models. *Nonlinear Processes in Geophysics*, *17*(6), 697–714.
1066 https://doi.org/10.5194/npg-17-697-2010

1067 Serinaldi, F., & Kilsby, C. G. (2014). Rainfall extremes: Toward reconciliation after the battle of
1068 distributions. *Water Resources Research*, *50*(1), 336–352.
1069 https://doi.org/10.1002/2013WR014211

1070 Sharma, D., Das Gupta, A., & Babel, M. S. (2007). Spatial disaggregation of bias-corrected
1071 GCM precipitation for improved hydrologic simulation: Ping River Basin, Thailand.
1072 *Hydrology and Earth System Sciences*, *11*(4), 1373–1390. https://doi.org/10.5194/hess-
1073 11-1373-2007

1074 Sigrist, F., Künsch, H. R., & Stahel, W. A. (2012). A Dynamic Nonstationary Spatio-Temporal
1075 Model for Short Term Prediction of Precipitation. *The Annals of Applied Statistics*, *6*(4),
1076 1452–1477.

1077 Smith, A. B., & Katz, R. W. (2013). US billion-dollar weather and climate disasters: data
1078 sources, trends, accuracy and biases. *Natural Hazards*, *67*(2), 387–410.
1079 https://doi.org/10.1007/s11069-013-0566-5

1080 Smith, J. A., & Baeck, M. L. (2015). “Prophetic vision, vivid imagination”: The 1927
1081 Mississippi River flood. *Water Resources Research*, *51*(12), 9964–9994.
1082 https://doi.org/10.1002/2015WR017927

1083 Smith, T. J., Pascal Bourgault, Florenz A. P. Hollebrandse, Sam Gillespie, William Asquith, & J.
1084 R. M. Hosking. (2023). lmoments3 (Version 1.0.5). Retrieved from
1085 https://lmoments3.readthedocs.io/en/stable/index.html

1086 Sperandei, S. (2014). Understanding logistic regression analysis. *Biochemia Medica*, *24*(1), 12–
1087 18. https://doi.org/10.11613/BM.2014.003

1088 Stacy, E. W. (1962). A Generalization of the Gamma Distribution. *The Annals of Mathematical*
1089 *Statistics*, *33*(3), 1187–1192.

1090 Storvik, G., Frigessi, A., & Hirst, D. (2002). Stationary space-time Gaussian fields and their time
1091 autoregressive representation. *Statistical Modelling*, *2*(2), 139–161.
1092 https://doi.org/10.1191/1471082x02st029oa

1093 Su, Y., Smith, J. A., & Villarini, G. (2023). The Hydrometeorology of Extreme Floods in the
1094 Lower Mississippi River. *Journal of Hydrometeorology*, *24*(2), 203–219.
1095 https://doi.org/10.1175/JHM-D-22-0024.1

1096 Trinh, B. N., Thielen-del Pozo, J., & Thirel, G. (2013). The reduction continuous rank
1097 probability score for evaluating discharge forecasts from hydrological ensemble
1098 prediction systems. *Atmospheric Science Letters*, *14*(2), 61–65.
1099 https://doi.org/10.1002/asl2.417

1100 Veneziano, D., Langousis, A., & Furcolo, P. (2006). Multifractality and rainfall extremes: A
1101 review. *Water Resources Research*, *42*(6). https://doi.org/10.1029/2005WR004716

1102 Virtanen, P., Gommers, R., Oliphant, T. E., Haberland, M., Reddy, T., Cournapeau, D., et al.
1103 (2020). SciPy 1.0: Fundamental algorithms for scientific computing in python. *Nature*
1104 *Methods*, *17*, 261–272. https://doi.org/10.1038/s41592-019-0686-2

1105 Vischel, T., Quantin, G., Lebel, T., Viarre, J., Gosset, M., Cazenave, F., & Panthou, G. (2011).
1106 Generation of High-Resolution Rain Fields in West Africa: Evaluation of Dynamic
1107 Interpolation Methods. *Journal of Hydrometeorology*, *12*(6), 1465–1482.
1108 https://doi.org/10.1175/JHM-D-10-05015.1

1109 Vrac, M., Drobinski, P., Merlo, A., Herrmann, M., Lavaysse, C., Li, L., & Somot, S. (2012).
1110 Dynamical and statistical downscaling of the French Mediterranean climate: uncertainty
1111 assessment. *Natural Hazards and Earth System Sciences*, *12*(9), 2769–2784.
1112 https://doi.org/10.5194/nhess-12-2769-2012

1113 Vrac, Mathieu, & Thao, S. (2020). R^2D^2 v2.0: accounting for temporal dependences in
1114 multivariate bias correction via analogue rank resampling. *Geoscientific Model*
1115 *Development*, *13*(11), 5367–5387. https://doi.org/10.5194/gmd-13-5367-2020

1116 Waymire, E., & Gupta, V. K. (1981). The mathematical structure of rainfall representations: 1. A
1117 review of the stochastic rainfall models. *Water Resources Research*, *17*(5), 1261–1272.
1118 https://doi.org/10.1029/WR017i005p01261

1119 Waymire, E., Gupta, V. K., & Rodriguez-Iturbe, I. (1984). A Spectral Theory of Rainfall
1120 Intensity at the Meso-β Scale. *Water Resources Research*, *20*(10), 1453–1465.
1121 https://doi.org/10.1029/WR020i010p01453

Wilks, D., & Wilby, R. (1999). The weather generation game: a review of stochastic weather models. https://doi.org/10.1177/030913339902300302

Wright, D., Smith, J., & Baeck, M. (2014). Flood Frequency Analysis Using Radar Rainfall Fields and Stochastic Storm Transposition. *Water Resources Research*, *50*, 1592–1615. https://doi.org/10.1002/2013WR014224

Yu, G., Wright, D. B., & Li, Z. (2020). The Upper Tail of Precipitation in Convection-Permitting Regional Climate Models and Their Utility in Nonstationary Rainfall and Flood Frequency Analysis. *Earth's Future*, *8*(10). https://doi.org/10.1029/2020EF001613

Zhang, C., Yang, X., Tang, Y., & Zhang, W. (2020). Learning to Generate Radar Image Sequences Using Two-Stage Generative Adversarial Networks. *IEEE Geoscience and Remote Sensing Letters*, *17*(3), 401–405. https://doi.org/10.1109/LGRS.2019.2922326

Zhang, X., Zwiers, F. W., Li, G., Wan, H., & Cannon, A. J. (2017). Complexity in estimating past and future extreme short-duration rainfall. *Nature Geoscience*, *10*(4), 255–259. https://doi.org/10.1038/ngeo2911

Zhuang, J., Dussin, R., Jüling, A., & Rasp, S. (2020, March 6). xESMF: Universal Regridder for Geospatial Data. Zenodo. https://doi.org/10.5281/zenodo.1134365

References From the Supporting Information

Famien, A. M., Janicot, S., Ochou, A. D., Vrac, M., Defrance, D., Sultan, B., & Noël, T. (2018). A bias-corrected CMIP5 dataset for Africa using the CDF-t method – a contribution to

agricultural impact studies. Earth System Dynamics, 9(1), 313–338. https://doi.org/10.5194/esd-9-313-2018

Liu, Y., & Wright, D. B. (2022). A storm-centered multivariate modeling of extreme precipitation frequency based on atmospheric water balance. Hydrology and Earth System Sciences, 26(20), 5241–5267. https://doi.org/10.5194/hess-26-5241-2022

Vrac, M., Drobinski, P., Merlo, A., Herrmann, M., Lavaysse, C., Li, L., & Somot, S. (2012). Dynamical and statistical downscaling of the French Mediterranean climate: uncertainty assessment. Natural Hazards and Earth System Sciences, 12(9), 2769–2784. https://doi.org/10.5194/nhess-12-2769-2012